

See discussions, stats, and author profiles for this publication at: <https://www.researchgate.net/publication/263954408>

# Enhanced Hydrogen Storage Kinetics and Stability by Synergistic Effects of in Situ Formed CeH<sub>2.73</sub> and Ni in CeH<sub>2.73</sub>-MgH<sub>2</sub>-Ni Nanocomposites

ARTICLE in THE JOURNAL OF PHYSICAL CHEMISTRY C · APRIL 2014

Impact Factor: 4.77 · DOI: 10.1021/jp500439n

CITATIONS

37

READS

92

8 AUTHORS, INCLUDING:



[Liuzhang Ouyang](#)

South China University of Technology

152 PUBLICATIONS 1,520 CITATIONS

SEE PROFILE



[M. Zhu](#)

South China University of Technology

235 PUBLICATIONS 2,722 CITATIONS

SEE PROFILE



[Jiangwen Liu](#)

South China University of Technology

101 PUBLICATIONS 729 CITATIONS

SEE PROFILE



[X. D. Yao](#)

Griffith University

3 PUBLICATIONS 66 CITATIONS

SEE PROFILE

# Enhanced Hydrogen Storage Kinetics and Stability by Synergistic Effects of *in Situ* Formed $\text{CeH}_{2.73}$ and Ni in $\text{CeH}_{2.73}$ - $\text{MgH}_2$ -Ni Nanocomposites

L. Z. Ouyang,<sup>†,‡</sup> X. S. Yang,<sup>†</sup> M. Zhu,<sup>\*,†,‡,§</sup> J. W. Liu,<sup>†,‡</sup> H. W. Dong,<sup>†</sup> D. L. Sun,<sup>‡</sup> J. Zou,<sup>§</sup> and X. D. Yao<sup>\*,||,‡</sup>

<sup>†</sup>School of Materials Science and Engineering, South China University of Technology, Guangzhou 510641, People's Republic of China

<sup>‡</sup>Department of Materials Science, Fudan University, Shanghai 200433, People's Republic of China

<sup>§</sup>Materials Engineering and Centre for Microscopy and Microanalysis, The University of Queensland, St. Lucia, QLD 4072, Australia

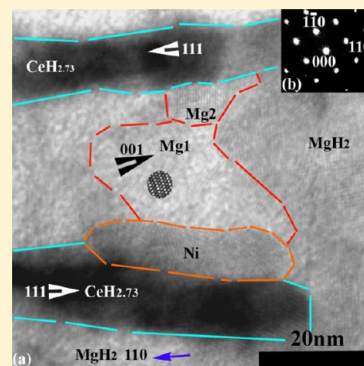
<sup>||</sup>School of Biomolecular and Physical Sciences, Griffith University, Nathan, QLD 4111, Australia

<sup>‡</sup>Key Laboratory of Advanced Energy Storage Materials of Guangdong Province, South China University of Technology, Guangzhou 510641, People's Republic of China

<sup>#</sup>Australia-China Joint Laboratory for Energy & Environmental Materials, Griffith University, Nathan, QLD 4111, Australia

## S Supporting Information

**ABSTRACT:** Mg-based materials are promising candidates for high capacity hydrogen storage. However, their poor hydrogenation/dehydrogenation kinetics and high desorption temperature are the main obstacles to their applications. This paper reports a method for *in situ* formation of cycle stable  $\text{CeH}_{2.73}$ - $\text{MgH}_2$ -Ni nanocomposites, from the hydrogenation of as-melt  $\text{Mg}_{80}\text{Ce}_{18}\text{Ni}_2$  alloy, with excellent hydrogen storage performance. The nanocomposites demonstrate reversible hydrogen storage capacity of more than 4.0 wt %, at a low desorption temperature with fast kinetics and long cycle life. The temperature for the full hydrogenation/dehydrogenation cycle of the composites is significantly decreased to 505 K, which is about 100 K lower than that for pure Mg. The hydrogen desorption activation energy is  $63 \pm 3$  kJ/mol  $\text{H}_2$  for the composites, which is significantly lower than those of  $\text{Mg}_3\text{Ce}$  alloy and pure Mg ( $104 \pm 7$  and  $158 \pm 2$  kJ/mol  $\text{H}_2$ , respectively). X-ray diffraction and transmission electron microscopy have been used to reveal the mechanism that delivers this excellent cycle stability and fast hydriding/dehydriding kinetics. It is found that the hydriding/dehydriding process is catalyzed by the combination of *in situ* formed extremely fine  $\text{CeH}_2/\text{CeH}_{2.73}$  and Ni to Mg/ $\text{MgH}_2$ . In addition, this nanocomposite structure can effectively suppress Mg/ $\text{MgH}_2$  grain growth and enable the material to maintain its high performance for more than 500 hydrogenation dehydrogenation cycles.



## 1. INTRODUCTION

High-density hydrogen storage is a key issue to be solved to facilitate large-scale applications of hydrogen energy.<sup>1</sup> Because of their high storage capacities, abundance, and low cost, Mg-based materials have attracted extensive attention as promising candidates for hydrogen storage.<sup>2</sup> However, Mg-based hydrides have slow dehydrogenation kinetics and relatively high desorption temperatures due to the highly stable Mg-H bond.<sup>3</sup> Therefore, considerable efforts have been made to improve the kinetics of Mg-based alloys at ambient temperatures by means of microstructure manipulation,<sup>4</sup> catalysis,<sup>5</sup> nanoscaling,<sup>6</sup> and employment of composites.<sup>7</sup>

A great success in kinetic modification has been achieved by preparing nanocrystalline magnesium hydrides including nanoparticles, nanofilms, and nanowires, which could make the hydrogen absorption and desorption easier at relatively low temperatures.<sup>12–16</sup> Magnesium nanowires having a uniform

diameter of 30–50 nm can absorb 2.93 wt % hydrogen at 373 K within 30 min and release as high as 3.28 wt % hydrogen within 30 min at 473 K, at which bulk Mg/ $\text{MgH}_2$  cannot release any hydrogen.<sup>11</sup> The thermal hydrogen desorption from  $\text{MgH}_2$  nanoparticles with primary particle size of <10 nm can start to release hydrogen at remarkably low temperatures of 350 K.<sup>14</sup> These improvements are attributed to the large grain boundary and surface area brought by small particle sizes, which provides larger surface for reactions with the hydrogen and short length of the hydrogen diffusion into the matrix of the materials.<sup>17</sup> Although the prepared nanoparticles show great promise, the kinetic properties and cyclic stabilities of these materials usually degrade rapidly during the hydrogenation/dehydrogenation

Received: January 15, 2014

Revised: March 20, 2014

Published: March 21, 2014

cycles due to the grain growth of nanocrystalline magnesium.<sup>3</sup> Denys et al.<sup>18</sup> reported that Mg crystallite sizes increased from 7 nm for ball-milled  $\text{MgH}_2$  to over 150 nm during thermal desorption at 623 K, which mitigated the kinetics of the transformations. Furthermore, absorption and desorption at lower temperatures are still insufficient for on board usage due to the low dissociation ability of metallic Mg for hydrogen molecules.<sup>19,20</sup> To overcome these problems, catalysts with a better H-dissociation ability have been applied to catalyze nanocrystalline  $\text{MgH}_2$  desorption,<sup>21–24</sup> pin the nanoscale microstructure, and inhibit grain growth.<sup>25–27</sup> Yu et al. reported that  $\text{MgH}_2$  catalyzed by BCC alloys with an average particle size of a few micrometers showed a much lower dehydrogenation peak temperature (567 K) and activation energy (71.25 kJ/mol  $\text{H}_2$ ) than the pristine sample.<sup>21</sup> Guvendiren et al. observed that  $\text{MgH}_2$  with micrometer-sized graphite could store 4 wt % hydrogen in <7 min at 623 K and release hydrogen within 5 min at 673 K.<sup>22</sup> The catalytic effect becomes much more pronounced when the size of catalysts decreases due to the increased interfaces and shortened diffusion path. Jin et al. prepared a composite system of nanocrystalline  $\text{MgH}_2$  with fine and evenly dispersed nano-Nb hydride (less than 20 nm) by milling a mixture of  $\text{MgH}_2$  and 1 mol %  $\text{NbF}_5$ .<sup>23</sup> This NbH-catalyzed  $\text{MgH}_2$  desorbed 6.3 wt %  $\text{H}_2$  in 15 min and absorbed more than 90% of its initial hydrogen capacity within 5 min at 573 K. Moreover, this fast sorption kinetics was maintained after 10 cycles. Lu et al. synthesized a nanostructured  $\text{MgH}_2$ -0.1TiH<sub>2</sub> composite (5–10 nm of grain size) by using ultrahigh-energy and high-pressure mechanical milling, which could release around 4 wt % hydrogen even at a low temperature of 513 K within 20 min.<sup>24</sup> It is reported that the dehydrogenation enthalpy ( $\Delta H$ ) was also decreased from 75.6 to 68.5 kJ/mol due to its extremely fine grain size (5–10 nm). Actually, the desorption temperature is directly determined by the thermodynamics, e.g.  $T_{\text{des}} = \Delta H / \Delta S$ , where  $\Delta H$  is the enthalpy and  $\Delta S$  is the entropy. The milled  $\text{MgH}_2$ -0.1TiH<sub>2</sub> material also showed an excellent cyclic stability upon hydrogenation/dehydrogenation tests, in which there was only a little loss of hydrogen storage capacity after 80 cycles. Cuevas et al. demonstrated that the nano-TiH<sub>2</sub> phase could inhibit grain coarsening of Mg, which allows extended nucleation of the  $\text{MgH}_2$  phase in Mg nanoparticles before a continuous and blocking  $\text{MgH}_2$  hydride layer was formed.<sup>25</sup> Nano Pd catalyzed Mg thin films prepared by magnetron sputtering could even absorb hydrogen entirely at room temperature and dehydrogenate completely and rapidly in atmospheric pressure.<sup>16</sup> The pinning effect of catalyst interfaces was also found by the addition of Zr, Mn, and Ni.<sup>26,27</sup> Accordingly, it is very important to obtain a stable nanocrystalline  $\text{MgH}_2$  system with a homodispersed nanoscale catalyst for maintaining the excellent kinetic properties, e.g., synthesize the ultrafine particles of catalyst and keep the particle/grain of Mg-based nanocomposite from growing during dehydrogenation/hydrogenation.

It is suggested that *in situ* formed catalyst show higher catalytic activity and superior stability than those of the externally added catalyst due to the better homogeneity and finer particle sizes. Wang et al. found that mechanical milling of a NaH/Al mixture or  $\text{NaAlH}_4$  with metallic Ti powder resulted in the formation of *in situ* Ti hydrides,<sup>28</sup> acting as active species to catalyze the reversible dehydrogenation of  $\text{NaAlH}_4$ . *In situ* formed  $\text{MgH}_2$  also improved the reversibility of  $\text{LiBH}_4$ , the dehydrogenation products of which can be rehydrided under

moderate conditions, i.e., 673 K and 6.0 MPa of hydrogen pressure for 2 h without catalyst.<sup>29</sup> Gross et al. observed that the hydrogen absorption/desorption of  $\text{La}_2\text{Mg}_{17}$  was far more rapid than Mg due to the catalytic effect of *in situ* formed  $\text{LaH}_3$ .<sup>9</sup> Poletaev et al. showed that the disproportionation–recombination process of  $\text{La}_{1.80}\text{Mg}_{16.39}\text{Ni}_{1.01}$  alloy led to favorable kinetics for the hydrogen storage process due to the *in situ* formation of an  $\text{Mg}_2\text{Ni}$  phase.<sup>33</sup> Of these additives with positive effect, 3d transition metal Ni has been proved to be able to significantly lower the dissociation barrier.<sup>30,31</sup> However, in their cases, no pure Ni was generated by a disproportionation process of the  $\text{La}_{1.80}\text{Mg}_{16.39}\text{Ni}_{1.01}$  alloy, which may restrict the optimization of catalytic effect of Ni and  $\text{Mg}_2\text{Ni}$ . It has also been reported that the dissociation barrier is significantly lowered when Ni atoms are located on the surface of Mg, whereas the barrier remains essentially unaffected by Ni at the energetically favored inner layers.<sup>32</sup> This bottleneck problem might be solved by creating a stable nanostructure with a high density of *in situ* formed catalyst(Ni)/hydride interfaces, which may not only play an interfacial and catalytic role for hydrogen absorption/desorption but also inhibit phase growth of the nanocomposite during the hydrogenation/dehydrogenation process.

It is reported that metal hydrides ( $\text{MgH}_2$  and  $\text{LaH}_3$ ) provide a synergetic thermodynamic and kinetic destabilization on the dehydrogenation/hydrogenation process,<sup>34</sup> which is responsible for the distinct reduction in the operating temperatures of the as-prepared  $\text{LiBH}_4$ - $x\text{La}_2\text{Mg}_{17}$  composites. On the other hand, metal hydrides like  $\text{VH}_x$  may also work as a hydrogen pump during the dehydrogenation/hydrogenation in magnesium hydride system.<sup>35</sup> It is explained as that metal hydride chemisorbs hydrogen atoms and transfers them to the Mg–metal interfaces which acts as active nucleation sites for magnesium hydride, thus dramatically improving the kinetics properties. This effect is particularly significant for those *in situ* formed  $\text{REH}_{2-3}$  (where RE denotes a rare-earth element).<sup>36–45</sup> The magnesium-rich alloys  $\text{LnMg}$  ( $\text{Ln} = \text{La}, \text{Ce}$ , mischmetal),  $\text{La}_2\text{Mg}_{17}$ , and  $\text{Ce}_5\text{Mg}_{41}$  transform into  $\text{MgH}_2$  and the corresponding rare earth hydrides through studying their hydriding process. Moreover, the *in situ* formed rare earth hydrides act as catalysts in the dehydriding/hydriding process of magnesium.<sup>36</sup> It is also reported that  $\text{La}_2\text{Mg}_{17}$ ,<sup>37</sup>  $\text{CeMg}_{12}$ ,  $\text{LaMg}_{11}$ ,  $\text{Ce}_5\text{Mg}_{41}$ , and  $\text{Mg}_{24}\text{Y}_5$  could absorb hydrogen even at a temperature as low as 473 K to form  $\text{MgH}_2$ - $\text{REH}_{2-3}$  composites.<sup>37–41</sup> Our previous studies have indicated that  $\text{Mg}_3\text{RE}$ -based alloys can absorb hydrogen at room temperature.<sup>42,43</sup> Furthermore, the *in situ* formed hydrides even showed a synergetic effect on improving the kinetic properties. Sun et al. suggested a synergetic effect of hydrogenated  $\text{Mg}_3\text{La}$  and  $\text{TiCl}_3$  on the dehydrogenation of  $\text{LiBH}_4$ .<sup>45</sup> Further study showed that nanostructure Mg–Ce system had much faster kinetics and lower  $\text{MgH}_2$  desorption activation energy.

Inspired by these results, it is anticipated to synthesize the  $\text{MgH}_2$ -based composites catalyzed by *in situ* formed  $\text{CeH}_{2.73}$  and Ni with controlled shape and distribution. The *in situ* formed  $\text{CeH}_{2.73}$  and Ni may show a synergetic effect on enhancing the hydrogen storage kinetics and stability. Indeed, it has been reported that  $\text{CeMgNi}_4$  may react with hydrogen to form cerium hydride and pure Ni. It is difficult to form pure Ni due to the facile formation of  $\text{Mg}_2\text{Ni}$  during the hydrogenation process at above 633 K, but Ni can be stable in the Mg–RE–Ni system. The mechanism of the hydrogenation/dehydrogenation process of  $\text{MgH}_2$ ,  $\text{Mg}_2\text{NiH}_4$ , and  $\text{REH}_{2-3}$  has previously

been studied by *in situ* synchrotron X-ray diffraction (XRD) analysis.<sup>31,37</sup> However, to the best of our knowledge, no direct microstructural observations of the disproportionation reaction for hydrogen absorption on Mg-RE compounds or for the desorption process in Mg-RE-Ni alloys have hitherto been reported. In this study, we have designed an Mg-rich  $\text{Mg}_3\text{Ce}$ -based  $\text{Mg}_{80}\text{Ce}_{18}\text{Ni}_2$  alloy, in which Mg-Ce compounds and  $\text{CeMgNi}_4$  transformed into the *in situ* formed  $\text{CeH}_{2.73}$  and Ni-catalyzed  $\text{MgH}_2$  nanocomposites upon the first hydrogenation process.<sup>46</sup> This newly designed *in situ* catalyzed nanocomposite shows excellent hydrogen storage kinetics and stability. Through detailed structural and chemical characterization using electron microscopy, the fundamentals for the enhanced hydrogen storage kinetics and stability have been investigated.

## 2. EXPERIMENTAL SECTION

The Ni arises from the decomposition of  $\text{CeMgNi}_4$  may catalyze the hydrogen absorption/desorption of  $\text{MgH}_2$ - $\text{CeH}_{2.73}$  composite and prohibits  $\text{MgH}_2$  and  $\text{CeH}_{2.73}$  grains growth. Thus, the Mg-rich  $\text{Mg}_3\text{Ce}$ -based alloy embedded about 5.0 wt %  $\text{CeMgNi}_4$ , with the nominal composition of  $\text{Mg}_{80}\text{Ce}_{18}\text{Ni}_2$  alloy, was prepared by induction melting in a MgO crucible under an argon atmosphere using the raw materials Mg, Ce, and Ni with purity of 99.9%. The theoretical hydrogen storage capacity is about 4.0 wt %. About 5 wt % extra Mg was added to compensate for the evaporation loss of Mg. According to EDX analysis, the composition of the as-melted  $\text{Mg}_{80}\text{Ce}_{18}\text{Ni}_2$  alloy was 80.7 at. % Mg, 17.5 at. % Ce, and 1.8 at. % Ni. For comparison,  $\text{Mg}_3\text{Ce}$  compound was also prepared in the same way. The composition of the as-melted  $\text{Mg}_3\text{Ce}$  compound was 72.3 at. % Mg and 27.7 at. % Ce.

The  $\text{Mg}_3\text{Ce}$  and  $\text{Mg}_{80}\text{Ce}_{18}\text{Ni}_2$  ingots obtained were individually mechanically pulverized in a steel vial and then put into a gas reaction controller (Advanced Materials Corporation) to measure the hydrogen absorption and desorption properties by evaluating pressure-composition isotherms (PCI) and kinetics at different temperatures. The dehydrogenation processes were performed under an initial state of vacuum (0.1 bar), which is widely accepted by most of previous studies, so the results derived can be comparable with literature reports. The sample masses for the PCI measurement were 1.731 and 1.214 g for the  $\text{Mg}_3\text{Ce}$  and  $\text{Mg}_{80}\text{Ce}_{18}\text{Ni}_2$  alloys, respectively. As the  $\text{MgH}_2$  and  $\text{CeH}_{2.73}$  formed *in situ* from hydrogenated  $\text{Mg}_3\text{Ce}$  and  $\text{Mg}_{80}\text{Ce}_{18}\text{Ni}_2$ , the two hydrogenated alloys are also referred to as *in situ* formed  $\text{MgH}_2$ - $\text{CeH}_{2.73}$  and  $\text{MgH}_2$ - $\text{CeH}_{2.73}$ -Ni composites, respectively. To examine the stability of the  $\text{MgH}_2$ - $\text{CeH}_{2.73}$ -Ni composite, cycling was repeated 505 times between the dehydrogenation under  $10^{-2}$  Pa around 570 K and hydrogenation under 3.5 MPa at room temperature. All samples were handled in an argon-filled glovebox where water and oxygen levels were below 2 ppm. The dehydrogenation enthalpy  $\Delta H$  and entropy  $\Delta S$  of the alloys were determined from the PCI data by using the van't Hoff equation,<sup>44</sup> where the  $\text{H}_2$  pressure at the midpoint of the desorption pressure plateau of the PCI curves was taken as the plateau pressure since it was not completely flat.

The evolution of the phase structures of the fabricated structures was comprehensively characterized. To determine the phase structure of the as-melted alloy and phase transformation after hydriding and dehydriding, X-ray diffraction (XRD) measurements were carried out on a Philips X'Pert MPD X-ray diffractometer with Cu K $\alpha$  radiation. A scanning rate of 0.02°/s was used in the  $2\theta$  range from 20° to

90°. The powder samples were covered with paraffin oil to prevent oxidation during measurements. The XRD profiles were analyzed with the Rietveld refinement program RIETAN-2000 to determine the phase lattice constant and phase relative content. The morphological characteristics of fabricated structures were studied by field emission scanning electron microscopy (FE-SEM, JEOL XL-30), and their structural and chemical characteristics were investigated using by transmission electron microscopy (TEM, JEOL-2100 equipped with an energy dispersive spectroscopy (EDS) system with an operating voltage of 200 kV). In order to clarify the hydrogenation mechanism, some samples were either partially hydrogenated or dehydrogenated and evaluated with a particular content of hydrogen by controlling the PCI measuring process. The alloy compositions were also assessed using inductively coupled plasma optical emission spectrometry.

## 3. RESULTS AND DISCUSSION

### 3.1. Formation of $\text{CeH}_{2.73}$ - $\text{MgH}_2$ -Ni Nanocomposites.

Figure 1a shows the Rietveld refinement of the observed XRD patterns of the as-melted  $\text{Mg}_{80}\text{Ce}_{18}\text{Ni}_2$  alloy. It is composed of

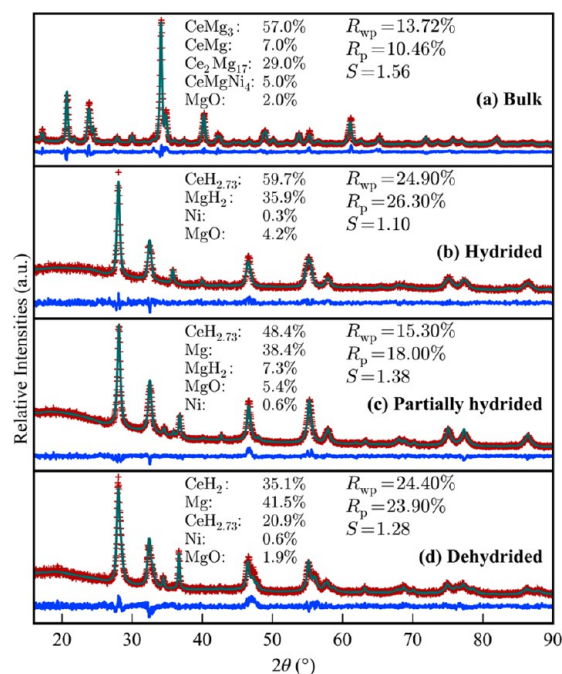


**Figure 1.** (a) Rietveld refinement on the observed XRD pattern of the as-melted  $\text{Mg}_{80}\text{Ce}_{18}\text{Ni}_2$  alloy.  $\text{Mg}_{80}\text{Ce}_{18}\text{Ni}_2$  alloy is composed of  $\text{Mg}_3\text{Ce}$  phase (57 wt %),  $\text{Ce}_2\text{Mg}_{17}$  phase (29 wt %),  $\text{CeMg}$  (7 wt %),  $\text{CeMgNi}_4$  (5 wt %), and a small amount of MgO (2 wt %). (b) Rietveld refinement on the observed XRD pattern of the  $\text{MgH}_2$ - $\text{CeH}_{2.73}$ -Ni composite hydrogenated from  $\text{Mg}_{80}\text{Ce}_{18}\text{Ni}_2$  alloy. The hydrogenated  $\text{Mg}_{80}\text{Ce}_{18}\text{Ni}_2$  alloy is composed of  $\text{MgH}_2$ ,  $\text{CeH}_{2.73}$ , Ni, and a small amount of MgO. (c) Rietveld refinement on the observed XRD pattern of the partially hydrogenated  $\text{Mg}_{80}\text{Ce}_{18}\text{Ni}_2$  alloy. The partially hydrogenated  $\text{Mg}_{80}\text{Ce}_{18}\text{Ni}_2$  alloy was composed of  $\text{CeH}_{2.73}$ ,  $\text{MgH}_2$ , and Mg phases, suggesting that the  $\text{CeH}_{2.73}$  and Mg phases were first formed and then transformed to the  $\text{CeH}_{2.73}$ - $\text{MgH}_2$ -Ni composites by the subsequent hydriding of Mg during hydrogenation. (d) Rietveld refinement on the observed XRD pattern of the dehydrogenated  $\text{MgH}_2$ - $\text{CeH}_{2.73}$ -Ni composite. In the dehydrogenation process, the *in situ* formed  $\text{CeH}_{2.73}$ - $\text{MgH}_2$ -Ni composites transform into  $\text{Mg}$ - $\text{CeH}_{2.73}$ - $\text{CeH}_2$ -Ni composites where Ni still remains unchanged.



Mg<sub>3</sub>Ce, Ce<sub>2</sub>Mg<sub>17</sub>, CeMg, and CeMgNi<sub>4</sub> phases and a small amount of MgO, with weight percentage of 57%, 29%, 7%, 5%, and 2%, respectively. This indicates that most of the Ni existed in the CeMgNi<sub>4</sub> phase in the as-prepared Mg<sub>80</sub>Ce<sub>18</sub>Ni<sub>2</sub> alloy. The lattice constant of Mg<sub>3</sub>Ce phase is 0.742(4) nm, which is very close to that in the as-melted Mg<sub>3</sub>Ce compound (0.744(8) nm). This confirmed that very rare Ni dissolved in the Mg<sub>3</sub>Ce compound.

Figure 1b shows the Rietveld refinement of the observed XRD patterns taken from hydrogenated Mg<sub>80</sub>Ce<sub>18</sub>Ni<sub>2</sub> alloy, in which the diffraction peaks raised from the Mg<sub>3</sub>Ce, Ce<sub>2</sub>Mg<sub>17</sub>, CeMg, and CeMgNi<sub>4</sub> phases disappeared, but new diffraction peaks associated with CeH<sub>2.73</sub>, MgH<sub>2</sub>, and Ni phases appeared. It indicates that the Mg<sub>80</sub>Ce<sub>18</sub>Ni<sub>2</sub> alloy fully reacted with hydrogen and transformed to MgH<sub>2</sub>, CeH<sub>2.73</sub>, and pure Ni, which is the same disproportionation reaction as that in the Mg<sub>3</sub>RE alloy.<sup>43,44</sup> Thus, CeMgNi<sub>4</sub> reacted with hydrogen and transformed to MgH<sub>2</sub> and CeH<sub>2.73</sub> and pure Ni. As the amount of Ni was very small, a detailed analysis was carried out using TEM (see below) in order to know exactly Ni shape and distribution. The easy decomposition of CeMgNi<sub>4</sub> was previously confirmed by X-ray diffraction, neutron diffraction, and *ab initio* calculations using pseudopotential and all-electron density functional theory (DFT) methods.<sup>46</sup>

In order to clarify the microstructure evolution during the hydrogenation of Mg<sub>80</sub>Ce<sub>18</sub>Ni<sub>2</sub>, XRD and TEM analyses were carried out on the partially and completely hydrogenated Mg<sub>80</sub>Ce<sub>18</sub>Ni<sub>2</sub> alloy, respectively. Figure 1c shows the Rietveld refinement of the observed XRD patterns taken from the partially hydrogenated Mg<sub>80</sub>Ce<sub>18</sub>Ni<sub>2</sub> alloy (here and after denoted as Mg<sub>80</sub>Ce<sub>18</sub>Ni<sub>2</sub>H<sub>54</sub>). Mg<sub>80</sub>Ce<sub>18</sub>Ni<sub>2</sub>H<sub>54</sub> was obtained by controlling the H<sub>2</sub> pressure applied on the AMC gas reaction controller using the Sievert method. The Mg<sub>80</sub>Ce<sub>18</sub>Ni<sub>2</sub>H<sub>54</sub> alloy was composed of CeH<sub>2.73</sub>, Mg, MgH<sub>2</sub>, and Ni phases. The existence of pure Mg suggests that the CeH<sub>2.73</sub>, Mg and Ni phases were first formed, and then Mg reacted with hydrogen and further transformed to the CeH<sub>2.73</sub>-MgH<sub>2</sub>-Ni composite during the hydrogenation process (as shown in Figure 1b). This is because rare earth (RE) elements have a higher affinity with hydrogen than Mg, resulting in preferential reaction of RE with hydrogen to form REH<sub>2-3</sub> than that of Mg to form MgH<sub>2</sub>. Thus, the phase analysis of partially hydrogenated Mg<sub>80</sub>Ce<sub>18</sub>Ni<sub>2</sub> alloy confirmed the formation of CeH<sub>2.73</sub> for the first step during the hydrogenation process.<sup>43,44</sup> Figure 1d shows the Rietveld refinement of the observed XRD patterns taken from the dehydrogenated CeH<sub>2.73</sub>-MgH<sub>2</sub>-Ni composite, in which the diffraction peaks of MgH<sub>2</sub> phases disappeared and the peaks for CeH<sub>2.73</sub> became relatively weaker, but the additional diffraction peaks can be indexed as CeH<sub>2</sub> and Mg. It is of interest that 62.7 wt % of CeH<sub>2.73</sub> has transformed to CeH<sub>2</sub> in this pure Ni-catalyzed CeH<sub>2.73</sub>-MgH<sub>2</sub>-Ni composite during the dehydrogenation process.

However, in the alloy without Ni, CeH<sub>2.73</sub> remained stable in the MgH<sub>2</sub>-CeH<sub>2.73</sub> composite, demonstrated by the phase transition of Mg<sub>3</sub>Ce compound in the dehydrogenation/hydrogenation process. As shown in Figure 2a,b, the as-melted alloy presented only a Mg<sub>3</sub>Ce phase (space group *Fm* $\bar{3}$ *m*) with a lattice constant of 0.744(8) nm, and it transformed to CeH<sub>2.73</sub> and MgH<sub>2</sub> phases by the disproportionation reaction in hydrogenation, in the same way as other Mg<sub>3</sub>RE-based alloys.<sup>43,44</sup> For the dehydrogenated alloy, as shown in Figure 2c, the diffraction peaks of Mg appeared which compensated for the disappearance of the MgH<sub>2</sub> peaks. The peaks of CeH<sub>2.73</sub>

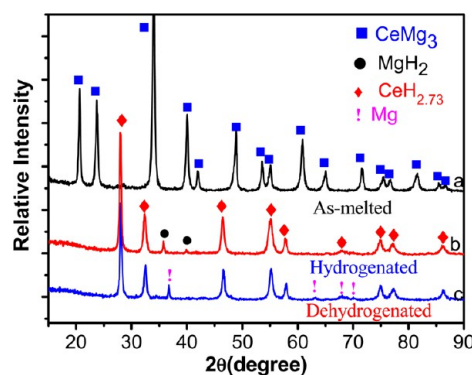


**Figure 2.** XRD patterns of (a) as-melted, (b) hydrogenated, and (c) dehydrogenated Mg<sub>3</sub>Ce alloy. Show that the MgH<sub>2</sub>-CeH<sub>2.73</sub> composite hydrogenated from the Mg<sub>3</sub>Ce alloy. The CeH<sub>2.73</sub> phase formed in hydrogenation remained stable during the dehydrogenation process and the effective component for hydrogen storage in the *in situ* formed MgH<sub>2</sub>-CeH<sub>2.73</sub> composites is MgH<sub>2</sub> during the following the dehydrogenation/hydrogenation cycle.

phase could be still clearly seen and its lattice constant remains unchanged at 0.553(2) nm. Therefore, in the following dehydrogenation/hydrogenation cycle, the effective component for hydrogen storage is only MgH<sub>2</sub> in the *in situ* formed MgH<sub>2</sub>-CeH<sub>2.73</sub> composite.

In fact, pure CeH<sub>2.73</sub> has high thermal stability and low dehydrogenation kinetics. The transformation of CeH<sub>2.73</sub> occurs over a broad range of temperatures (see the Supporting Information, Figure S1), ranging from room temperature up to 663 K. XRD analysis showed that the transformation from CeH<sub>2.73</sub> to CeH<sub>2</sub> was complete only up to 663 K by the temperature-programmed desorption (TPD) experiment (see the Supporting Information, Figure S2). This is similar to the situation for LaH<sub>3</sub> which transforms to LaH<sub>2</sub> from room temperature to 823 K and then starts to decompose at 873 K.<sup>47</sup> Obviously, the introduction of Ni may promote the transformation of CeH<sub>2.73</sub> to CeH<sub>2</sub> at 573 K in the CeH<sub>2.73</sub>-MgH<sub>2</sub>-Ni composite, which is about 100 K lower than that without the Ni. This is also a contribution to the hydrogen storage capacity (besides MgH<sub>2</sub>).

**3.2. Hydrogen Storage Capacity of CeH<sub>2.73</sub>-CeH<sub>2</sub>-Mg-Ni Composite.** Figure 3a–d shows the PCI curves of CeH<sub>2.73</sub>-MgH<sub>2</sub>-Ni composite measured at the different stages during the 500 cycles of the hydrogenation/dehydrogenation process, which proves that the reversible hydrogen storage capacity of about 4.0 wt %. Figure 3a shows the PCI curves at different temperatures measured among the first 70 cycles. It can be observed that only one main phase participates in the hydrogenation/dehydrogenation, e.g., MgH<sub>2</sub>/Mg. This is because that only a small amount of hydrogen is released from the transformation of CeH<sub>2.73</sub> to CeH<sub>2</sub>; thus, no obvious second plateau can be observed in the PCI curves. The hydrogen storage capacity decreases from the initial 4.03 wt % to 3.87 wt % at the 70th cycle with a retention rate of 96.75%. Figure 3b shows the PCI curves between the 90th and 170th cycles. The temperature is decreased gradually to the lowest temperature for the desorption of CeH<sub>2.73</sub>-MgH<sub>2</sub>-Ni composites, which is at 505 K. Furthermore, no kink, which existed in MgH<sub>2</sub>-CeH<sub>2.73</sub>, is observed for CeH<sub>2.73</sub>-MgH<sub>2</sub>-Ni composites, demonstrated that the hydrogenation/dehydrogenation kinetics of the CeH<sub>2.73</sub>-MgH<sub>2</sub>-Ni composites is much better than that of MgH<sub>2</sub>-CeH<sub>2.73</sub> composites due to the introduction of Ni.

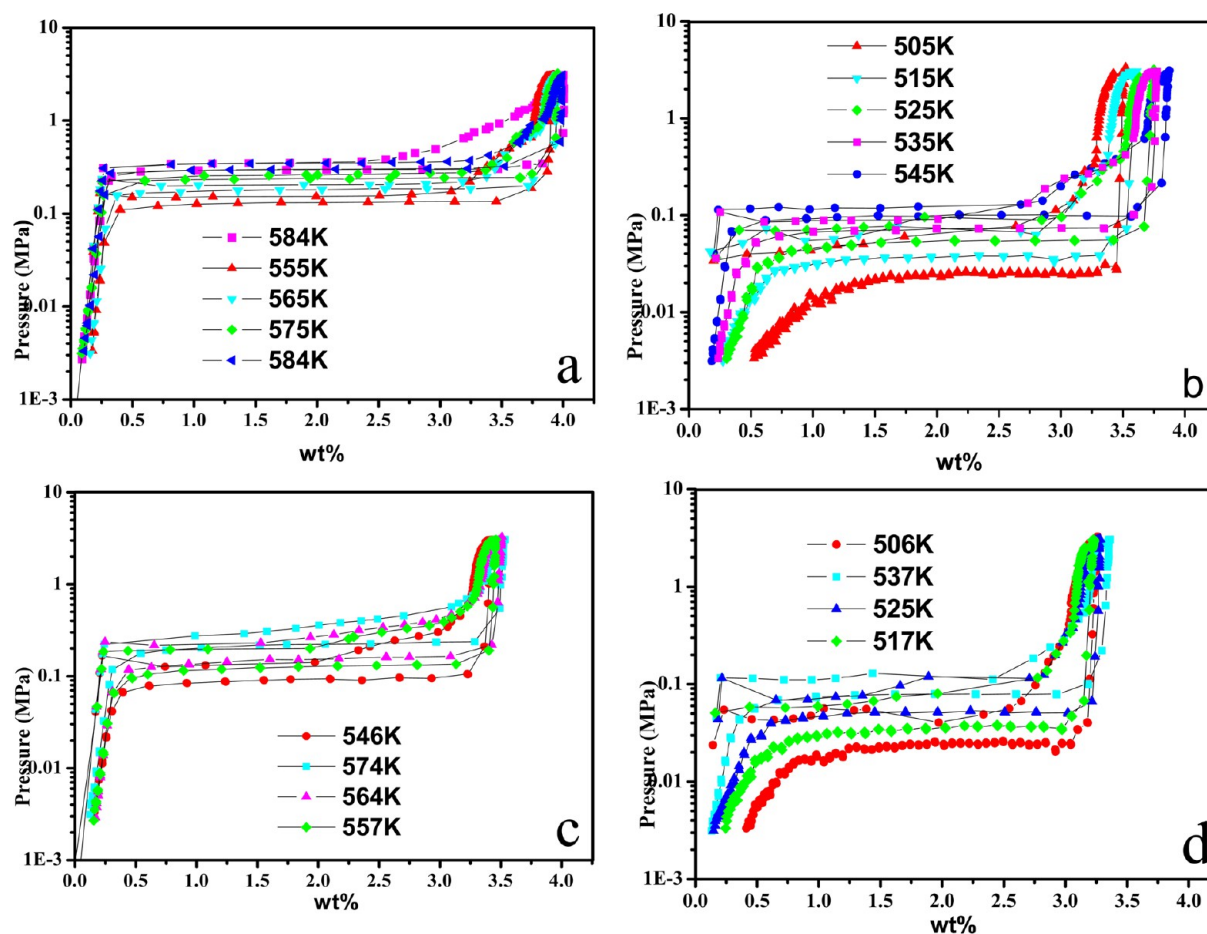


**Figure 3.** PCI curves of  $\text{Mg}_{80}\text{Ce}_{18}\text{Ni}_2$  alloy measured during the 500 cycle's dehydrogenation/hydrogenation process: (a) the first 70 cycles; (b) among the 90–170 cycles; (c) among 250–320 cycles; (d) among 350–500 cycles. The hydrogen storage capacity decreases from the maximum being 4.03 wt % to 3.23 wt % after 500 cycles. The plateaus of hydrogen absorption and desorption are flat, indicating that only one phase transformation during the dehydrogenation/hydrogenation process, which should be correspond to the phase transformation between Mg and  $\text{MgH}_2$ .

After 250 cycles, the hydrogen storage capacity for  $\text{CeH}_{2.73}\text{-MgH}_2\text{-Ni}$  composites gradually decreases to 3.50 wt %. In order to clarify whether the capacity is affected by the temperature, the PCI measurement was undertaken at a relatively higher temperature. Figure 3c shows the PCI curves at 546, 557, 564, and 574 K. The capacity is the same as that at a relatively lower temperature of 505 K. Figure 3d shows the PCI curves measured at different temperatures between the 350th and 500th cycles. During the last 150 cycles, the hydrogen storage capacity decreased from 3.32 to 3.23 wt %, and the degradation ratio was only 0.018%/cycle. It should be noted that the dehydrogenation/hydrogenation process is only by  $\text{MgH}_2/\text{Mg}$  cycling during all the cycles, and there is no sign of the formation of other Mg-based phases such as  $\text{Mg}_2\text{Ni}/\text{Mg}_2\text{NiH}_4$  phases from the PCI curves. The results described above show that  $\text{CeH}_{2.73}\text{-MgH}_2\text{-Ni}$  composite system is very stable during the dehydrogenation/hydrogenation cycling.

For comparison, PCI measurements of the *in situ* formed  $\text{MgH}_2\text{-CeH}_{2.73}$  composite were also carried out 578, 569, and 544 K as seen in Figure 4. The maximum hydrogen storage capacity of the *in situ* formed  $\text{MgH}_2\text{-CeH}_{2.73}$  composites is 2.49 wt % at 569 K, which is very close to the theoretical value of 2.56 wt %. There is only one plateau for each PCI curve, confirming again that the hydrogenation/dehydrogenation process corresponds to the transformation between Mg and

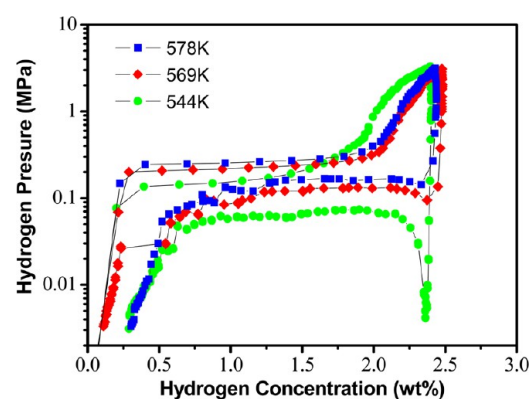


**Figure 4.** PCI curves of  $\text{CeH}_{2.73}\text{-MgH}_2$  composite measured at different temperatures. The maximum hydrogen storage capacity of the *in situ* formed  $\text{MgH}_2\text{-CeH}_{2.73}$  composites is 2.49 wt % at 569 K, which is very close to that theoretical value of 2.56 wt %.

$\text{MgH}_2$ . In addition, a kink is observed in the isotherm curve at 544 K, which is due to the fact that the desorption pressure is below of the balance (equilibrium) plateau. This is actually related to the sluggish desorption kinetics of the *in situ* formed  $\text{MgH}_2\text{-CeH}_{2.73}$  composites at the beginning of desorption and can be experimentally removed by setting a longer delay time in

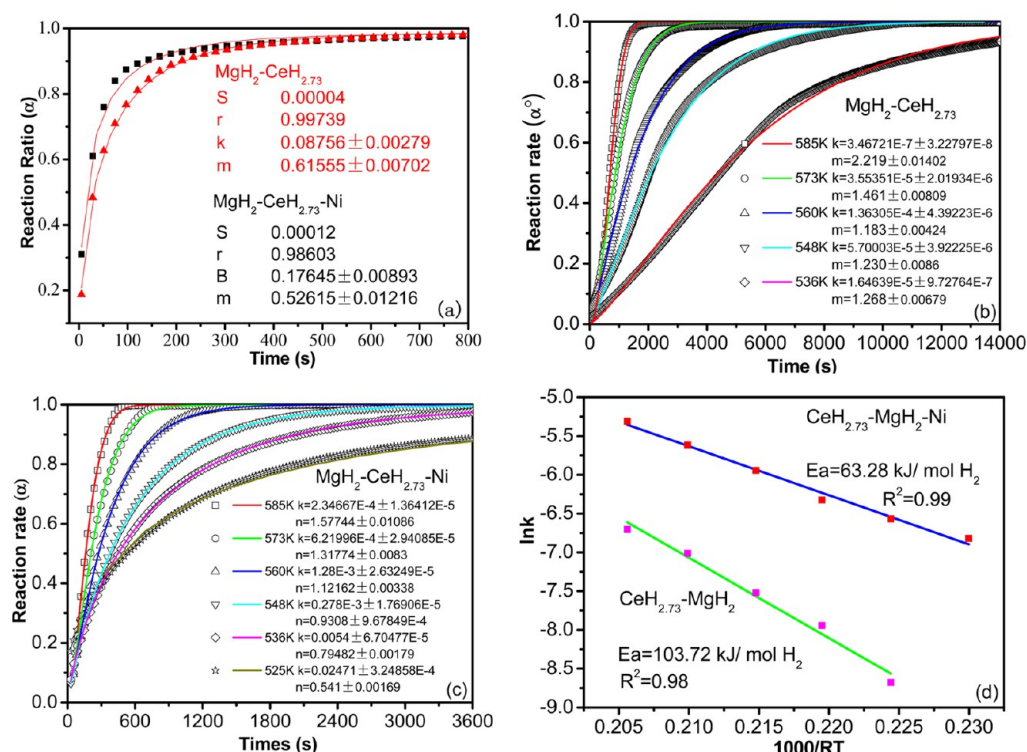


**Figure 5.** Hydrogen absorption/desorption kinetic curves for  $\text{CeH}_{2.73}\text{-MgH}_2$  and  $\text{CeH}_{2.73}\text{-MgH}_2\text{-Ni}$  composites. (a) Hydrogen absorption kinetic curves under 3.5 MPa hydrogen pressure at 298 K for  $\text{CeH}_{2.73}\text{-MgH}_2$  composite after 4 cycles and  $\text{CeH}_{2.73}\text{-MgH}_2\text{-Ni}$  composite after 1 cycle; the dehydrogenation kinetic curves for  $\text{CeH}_{2.73}\text{-MgH}_2$  (b) and  $\text{CeH}_{2.73}\text{-MgH}_2\text{-Ni}$ ; (c) composites at different temperature; (d) an Arrhenius plot of  $\ln k$  vs  $1/RT$  for  $\text{CeH}_{2.73}\text{-MgH}_2$  and  $\text{CeH}_{2.73}\text{-MgH}_2\text{-Ni}$  composites. The  $E_a$  for the  $\text{CeH}_{2.73}\text{-MgH}_2\text{-Ni}$  and  $\text{CeH}_{2.73}\text{-MgH}_2$  composites was  $63 \pm 3$  and  $104 \pm 7$  kJ/mol  $\text{H}_2$ , respectively. Obviously, the formation of  $\text{CeH}_{2.73}\text{-MgH}_2$  composites significantly lowers the apparent activation energy of  $\text{MgH}_2$ , and the  $\text{CeH}_{2.73}\text{-MgH}_2\text{-Ni}$  composites even further decreases it.

the PCI measurement. Even though the hydrogenation/dehydrogenation kinetics of the *in situ* formed  $\text{MgH}_2\text{-CeH}_{2.73}$  composites are much better than that of pure Mg, the presence of this kink implies that the desorption kinetics is still not good enough because quite a long delay time, 30 s, has already been set for our measurements. This may be because the catalytic effect of  $\text{CeH}_{2.73}$  phase is not sufficient and the particle size of the *in situ* formed  $\text{MgH}_2\text{-CeH}_{2.73}$  composites is not small enough to provide the high-density interface required for effective catalysis. Therefore, it is necessary to decrease the particle size and/or introduce additional catalyst to further improve the desorbing kinetics. This is confirmed in the  $\text{MgH}_2\text{-CeH}_{2.73}\text{-Ni}$  composites as shown in Figure 3.

**3.3. Kinetic and Thermodynamic Properties of the  $\text{CeH}_{2.73}\text{-MgH}_2\text{-Ni}$  Composites.** PCI measurements were carried out to evaluate the hydrogen desorption kinetics of the composites obtained by hydrogenating the  $\text{Mg}_{80}\text{Ce}_{18}\text{Ni}_2$  alloy. For comparison, the  $\text{Mg}_3\text{Ce}$  compound was also investigated under the same experimental conditions. Figure 5a shows the kinetic curves measured at 298 K for  $\text{CeH}_{2.73}\text{-MgH}_2$  after four cycles (several cycles are required to fully activate this composite) and the  $\text{CeH}_{2.73}\text{-MgH}_2\text{-Ni}$  after the first cycle, respectively. At 3.5 MPa and 298 K, the maximum capacity of the  $\text{CeH}_{2.73}\text{-MgH}_2\text{-Ni}$  composites is calculated as 3.92 wt %, while that of the hydrogenated  $\text{CeH}_{2.73}\text{-MgH}_2$  is 2.35 wt %. Evidently, the hydriding kinetics of the  $\text{CeH}_{2.73}\text{-MgH}_2\text{-Ni}$  composites is much faster than that of  $\text{CeH}_{2.73}\text{-MgH}_2$ ; e.g., the uptake time for reaching 90% of the maximum storage capacity is 2.5 and 4.1 min, respectively. To elucidate the reaction mechanism, the hydrogenation kinetic curves are

fitted with rate equations derived from different kinetic models, including a nucleation and growth model, an autocatalytic reaction model, and a phase-boundary-controlled reaction model, as illustrated in Figure 5a. It is found that the hydrogenation kinetic curves in both cases can be best fitted by the nucleation and growth model, as expressed by eq 1 (the Avrami–Erofeev equation):<sup>50</sup>

$$\alpha = 1 - \exp(-kt^m) \quad (1)$$

where  $\alpha$  is the fraction transformed at time  $t$ ,  $k$  is the rate constant, and  $m$  is the Avrami exponent. The fitted values of  $k$  and  $m$ , the error estimated by a factor of the standard error,  $S$ , and the correlation coefficient  $r$  are also given in Figure 5a. Although eq 1 describes the nucleation and growth model of the reaction, the rate-determining step of the reaction depends on the value of  $m$ . For instance, an  $m$  value of 0.62 corresponds to a one-dimensional diffusion process, while a value of 1.07 corresponds to a three-dimensional interface reaction process.<sup>51,52</sup> Here, the fitted values of  $m$  from the hydrogenation kinetic curves are about 0.62 for the hydrogenated  $\text{CeH}_{2.73}\text{-MgH}_2$  and 0.53 for the  $\text{CeH}_{2.73}\text{-MgH}_2\text{-Ni}$  composites, respectively, which are close to the aforementioned value of 0.62. This suggests that the hydriding processes of both alloys based on a one-dimensional growth.

In order to keep the grain size in the same order, the hydrogen desorption kinetics of both hydrogenated alloys were investigated at temperatures ranging from relatively high (585 K) to low (525 K) temperature, below the temperature for Mg/ $\text{MgH}_2$  grain growth (0.3–0.5 of the melting point). Under this condition, the measured results should represent the typical



kinetic properties via temperature, minimizing the effect of grain size variations. Figure Sb,c shows the hydrogen absorption/desorption kinetic curves for the respective alloys. The temperature dependences of the rate constants  $k$  are shown in the insets of Figure Sb,c. At 548 K, the maximum dehydrogenation capacity for CeH<sub>2.73</sub>-MgH<sub>2</sub> is 2.35 wt %, and that for the CeH<sub>2.73</sub>-MgH<sub>2</sub>-Ni composites is 3.88 wt %. The desorption time for reaching 90% of the maximum storage capacity are 96 and 25 min, respectively. Therefore, the hydrogen desorption rate of the CeH<sub>2.73</sub>-MgH<sub>2</sub>-Ni composites is almost 4 times faster than that of CeH<sub>2.73</sub>-MgH<sub>2</sub>. This is also demonstrated by the fitting results, whereby the  $k$  value for the CeH<sub>2.73</sub>-MgH<sub>2</sub>-Ni composites is about 3 times than that of CeH<sub>2.73</sub>-MgH<sub>2</sub> at various temperatures, as shown in Figure Sb,c.

To understand the improved dehydrogenation kinetics of the hydrogenated alloys, their apparent activation energies for desorption are estimated by fitting the experimental data. The hydrogen desorption kinetics and the associated apparent activation energies are quantitatively evaluated using the Arrhenius equation and the temperature dependence of the rate constant  $k$ :<sup>50</sup>

$$k = k_0 \exp(-E_a/RT) \quad (3)$$

where  $E_a$  is the apparent activation energy of the reaction process and  $k_0$  is a pre-exponential frequency factor. The values of  $k$  at different temperatures could be extracted from the fitted profiles in Figure Sb,c for the respective hydrogenated alloys. Figure Sd shows Arrhenius plots of  $\ln k$  versus  $1/RT$  for the hydrogenated alloys, from which the  $E_a$  values can be determined as  $63 \pm 3$  kJ/mol H<sub>2</sub> for CeH<sub>2.73</sub>-MgH<sub>2</sub>-Ni composites and  $104 \pm 7$  kJ/mol H<sub>2</sub> for CeH<sub>2.73</sub>-MgH<sub>2</sub>, respectively. An overview of experimentally determined apparent activation energies for dehydrogenations of MgH<sub>2</sub> and selected hydrides of Mg-based alloys is presented in Table 1. An apparent activation energy ( $E_a$ ) of about 158 kJ/mol H<sub>2</sub>

**Table 1. Apparent Activation Energies for Dehydrogenation of Magnesium-Based Alloys**

sample	particle size (nm)	$E_a$ (kJ mol <sup>-1</sup> )	ref
nano-MgH <sub>2</sub> -0.1TiH <sub>2</sub>	5–10	58.4	26
Pd-Mg-Pd films	not given	48	11
nano-MgH <sub>2</sub>	not given	127	2
nano-Mg	~10	60–120	15
Mg <sub>0.95</sub> Nb <sub>0.05</sub> H <sub>2</sub>	8.3	62–77	55
MgH <sub>2</sub> doped with CoCl <sub>2</sub>	not given	121.3	57
MgH <sub>2</sub> doped with NiCl <sub>2</sub>	not given	102.6	57
Mg <sub>0.95</sub> V <sub>0.05</sub> H <sub>2</sub>	not given	76	56
ball-milled Mg	not given	120	55
Mg	not given	156	55
Mg	not given	160	43
Mg	not given	158	this work
Mg <sub>3</sub> Ce		104 ± 7	this work
Mg <sub>80</sub> Ce <sub>18</sub> Ni <sub>2</sub>		63 ± 3	this work

for MgH<sub>2</sub>, which is similar to the values of 160 and 156 kJ/mol H<sub>2</sub> for nonmilled MgH<sub>2</sub> estimated by Huot et al. and Fernández et al.,<sup>52,53</sup> respectively, which confirms the reliability of our experimental measurements. The CeH<sub>2.73</sub>-MgH<sub>2</sub> clearly has much lower activation energy than that of MgH<sub>2</sub>,  $104 \pm 7$  kJ/mol H<sub>2</sub>, which indicates a much faster kinetics. The introduction of *in situ* formed Ni into the CeH<sub>2.73</sub>-MgH<sub>2</sub>-Ni composites leads to a further significant reduction in the

apparent activation energy. The present approach for lowering the activation energy is much more effective than the doping of MgH<sub>2</sub> with CoCl<sub>2</sub> or NiCl<sub>2</sub>, which gave values of 121.3 and 102.6 kJ/mol H<sub>2</sub>, respectively.<sup>54</sup> Indeed, the value of  $63 \pm 3$  kJ/mol H<sub>2</sub> is very close to that determined for Mg nanoparticles (~10 nm).<sup>1</sup> The above results clearly show that the  $E_a$  in the CeH<sub>2.73</sub>-MgH<sub>2</sub>-Ni composites is the smallest, which illustrates the reason for fastest kinetics of such composites.

In order to obtain the thermodynamic parameters of the dehydriding reaction of the CeH<sub>2.73</sub>-MgH<sub>2</sub>-Ni composites, the relationship between the dehydriding plateau pressure ( $P$ , in absolute atmosphere) and temperature ( $T$ , in K) in the PCI curves at different temperatures is plotted according to the van't Hoff equation:

$$\ln K^\ominus = -\Delta H/RT + \Delta S/R \quad (4)$$

where  $R$  is the gas constant (0.008 314 5 kJ/(K mol)),  $\Delta H$  (in kJ/mol H<sub>2</sub>) and  $\Delta S$  (in kJ/(K mol) H<sub>2</sub>) are enthalpy change and entropy change of the dehydriding reaction, respectively,  $K^\ominus$  is standard equilibrium constant, while  $K^\ominus = P_{H_2}$  in the dehydriding process and  $K^\ominus = 1/P_{H_2}$  in the hydriding reaction. Enthalpy change ( $\Delta H^{\text{des}}$ ) and entropy change ( $\Delta S^{\text{des}}$ ) for the dehydriding process of CeH<sub>2.73</sub>-MgH<sub>2</sub>-Ni composite after 10, 250, and 500 cycles are calculated (see the Supporting Information, Figure S3) and listed in Table 2. For an intuitive

**Table 2. Entropy Change ( $\Delta S^{\text{des}}$ ) and Enthalpy Change ( $\Delta H^{\text{des}}$ ) of Dehydriding Reactions and the Desorption Temperature Corresponding to the Decomposition Pressure of 1 bar for MgH<sub>2</sub>-CeH<sub>2.73</sub>-Ni Composite in Different Dehydrogenation/Hydrogenation Cycles**

cycles	temp corresponding to the decomposition press. of 1 atm. (K)	$\Delta H^{\text{des}}$ (kJ/mol H <sub>2</sub> )	$\Delta S^{\text{des}}$ (kJ/mol H <sub>2</sub> )
10	544.4	-76.1 ± 0.4	0.1395 ± 0.0003
250	547.6	-76.7 ± 0.4	0.1382 ± 0.0003
500	547.5	-76.9 ± 0.3	0.1405 ± 0.0003

comparison, the temperatures corresponding to the desorption pressure of 1 bar are also listed in Table 2. According to the data given in Table 2, the  $\Delta H^{\text{des}}$ ,  $\Delta S^{\text{des}}$ , and the desorption temperature are almost unchanged after different numbers of cycles, even up to 500 cycles. This result indicates that the thermodynamic properties of Mg-based alloys are basically unchanged by the *in situ* formation of the CeH<sub>2.73</sub>-MgH<sub>2</sub>-Ni nanocomposites.

**3.4. Cyclic and Structural Stability for the *in Situ* Formed CeH<sub>2.73</sub>-MgH<sub>2</sub>-Ni Nanocomposite.** As seen in Figure 6, the capacity degradation of the CeH<sub>2.73</sub>-MgH<sub>2</sub>-Ni composites is small. It decreases from the initial capacity of 4.03 wt % to 3.23 wt % with a retention rate of 80.0% after 500 cycles. The excellent cycle ability is due to the high structural stability of the *in situ* formed nanocomposites. It is confirmed by TEM and SEM observations that both the grain size and particle size of the *in situ* formed CeH<sub>2.73</sub>-MgH<sub>2</sub>-Ni nanocomposites are stable, and there is no obvious grain growth and particle agglomeration even at a temperature as high as 584 K, at which normally the recrystallization of pure Mg occurs. Figure 7 shows the SEM micrographs of the *in situ* formed CeH<sub>2.73</sub>-MgH<sub>2</sub>-Ni nanocomposites at 15 cycles and 500 cycles, respectively. Figure 7a shows that the particle size is about 100 nm at 15 cycles of hydrogenation/dehydrogenation. Figure 7b



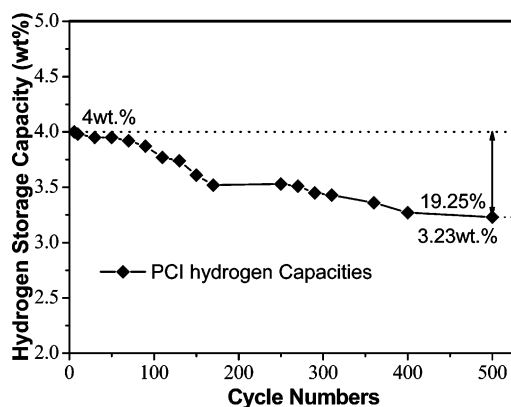


**Figure 6.** Evolution of the maximum hydrogen sorption capacities versus cycle times of  $\text{CeH}_{2.73}\text{-MgH}_2\text{-Ni}$  composite. Although the hydrogen storage capacity of the  $\text{CeH}_{2.73}\text{-MgH}_2\text{-Ni}$  composites degraded with increasing dehydrogenation/hydrogenation cycles, the degradation was very slow and the capacity decreased from the initial capacity of 4.03 wt % down to 3.23 wt % after 500 cycles, which corresponds to a high capacity retention rate of 80.1%.

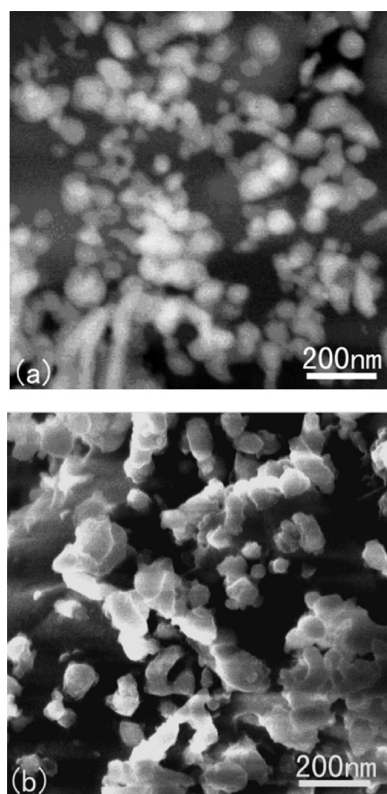


**Figure 7.** Scanning electron micrographs show the particle size of  $\text{CeH}_{2.73}\text{-MgH}_2\text{-Ni}$  composite after 15 cycles (a) and 500 cycles (b). After 500 cycles, the average particle size of the *in situ* formed  $\text{CeH}_{2.73}\text{-MgH}_2\text{-Ni}$  nanocomposites was not obviously grown compared to the average particle size after 15 cycles.

shows the average particle size after 500 cycles, which is in the same order compared to that at 15 cycles. The reason for this high stability is due to the unique lamellar structure of  $\text{MgH}_2$  and  $\text{CeH}_{2.73}$  and the existence of Ni nanoparticles at the boundary of the  $\text{Mg/MgH}_2$  and  $\text{CeH}_{2.73}$  phases (a detailed TEM analysis will be described in the next section). The nanoparticles are likely to prevent the movement of  $\text{Mg/MgH}_2$  and  $\text{CeH}_{2.73}$  boundaries.<sup>27</sup> Therefore, the catalytic effect and

improvement on the hydrogen desorption kinetics of  $\text{MgH}_2$  can be maintained due to the small grain growth.

In order to clarify the detailed structure, TEM observation is carried out for the dehydrogenated sample after 500 cycles. Figures 8a and 8b are TEM images of Mg particles in the

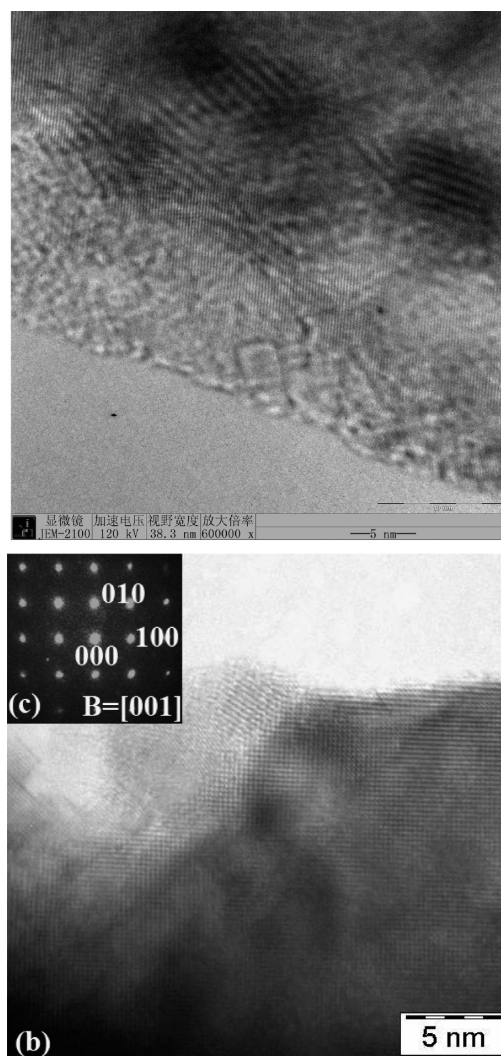


**Figure 8.** TEM images of Mg particle in the dehydrogenated  $\text{CeH}_{2.73}\text{-MgH}_2\text{-Ni}$  composites (a) after 505 cycles, (b) 5 cycles, and (c) selected diffraction pattern of  $\text{MgH}_2$ . An amorphous phase (according to SAED data, not shown) surrounds the Mg-based grains, corresponding to the  $\text{MgO}$  phase after 505 hydrogenation/dehydrogenation cycles.

$\text{CeH}_{2.73}\text{-MgH}_2\text{-Ni}$  composites after 505 cycles and 5 cycles, respectively. Figure 8a shows that there exists an amorphous  $\text{MgO}$  layer of about 4 nm thick on the surface of Mg particles. This  $\text{MgO}$  oxide layer forms by the reaction between oxygen impurity (gas oxides) that existed in the working hydrogen gas and  $\text{Mg/MgH}_2$ , leading to the loss of effective hydrogen storage capacity during the cycling. Figure 8b shows that the surfaces of Mg particles are clean, and no obvious oxide layer can be observed. Therefore, it is argued that the mechanism of cyclic degradation for the  $\text{CeH}_{2.73}\text{-MgH}_2\text{-Ni}$  composites is induced by oxidation but not by the changing of the nanocomposite structure. If it is assumed that the  $\text{MgH}_2$  particles are spherical with a diameter of 100 nm, as shown in Figure 7, the volume ratio of  $\text{MgO}$  to  $\text{Mg}$  was 12:88 in the sample of 500 cycles. This

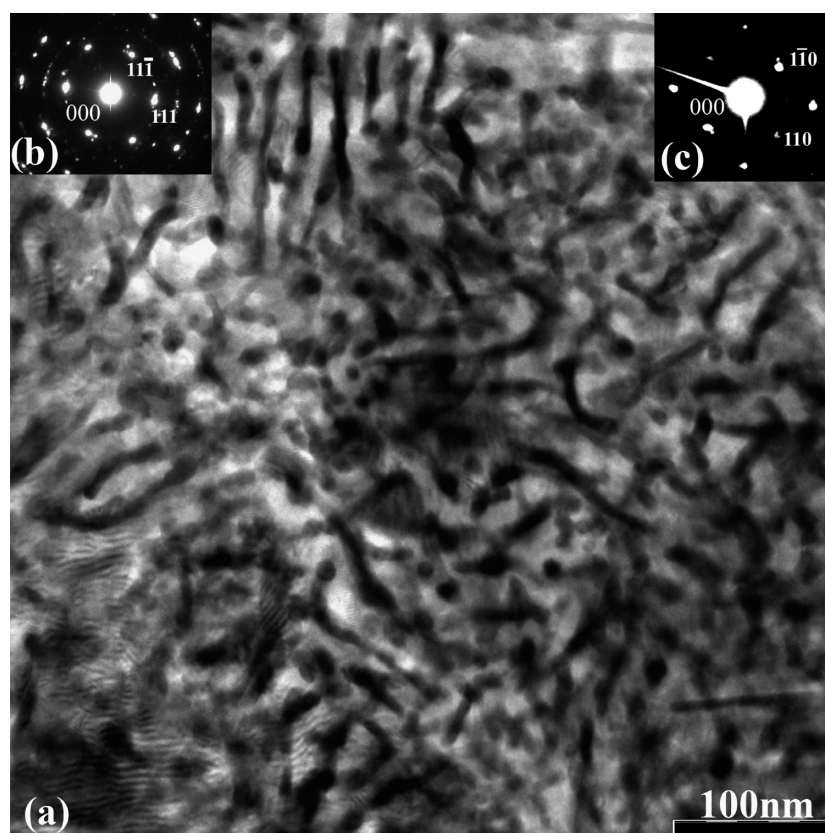


**Figure 9.** TEM images of the fully hydrogenated microstructure of in situ formed  $\text{CeH}_{2.73}$ -Ni- $\text{MgH}_2$  composite shows very fine plate-like or lamellar mixture of  $\text{MgH}_2$  and  $\text{CeH}_{2.73}$ . The structure includes a white matrix ( $\text{MgH}_2$  background) which includes thin plates of  $\text{CeH}_{2.73}$  (black). (a) Bright field image, (b) selected area diffraction patterns of  $\text{CeH}_{2.73}$  (zone axis  $[01\bar{1}]$ ), and (c) selected area diffraction patterns of tetragonal  $\text{MgH}_2$  (zone axis  $[001]$ ).

is accordance with retained 80.0% of hydrogen storage capacity after 500 cycles.

**3.5. Mechanism for the Hydrogenation/Dehydrogenation of  $\text{CeH}_{2.73}$ - $\text{MgH}_2$ -Ni Composites.** Summarizing the experimental results described above, it was found that (1) the  $\text{Mg}_{80}\text{Ce}_{18}\text{Ni}_2$  alloy transformed to the  $\text{CeH}_{2.73}$ , Mg, and Ni phases at first and then further transformed to the  $\text{CeH}_{2.73}$ - $\text{MgH}_2$ -Ni composites in the hydrogenation process; (2) compared to the  $\text{CeH}_{2.73}$ - $\text{MgH}_2$  composites, the  $\text{CeH}_{2.73}$ - $\text{MgH}_2$ -Ni composites have a lower desorption temperature and better absorption/desorption kinetic properties. In this section, the mechanism for the above two results is discussed by using high resolution TEM (HRTEM) analysis for the microstructure evolution of the *in situ* formed  $\text{CeH}_{2.73}$ - $\text{MgH}_2$ -Ni composites during hydrogenation/dehydrogenation. Figure 9a shows a bright field image of the fully hydrogenated microstructure of the  $\text{CeH}_{2.73}$ - $\text{MgH}_2$ -Ni composites. A very fine plate-like or lamellar mixture of  $\text{CeH}_{2.73}$  (dark) and  $\text{MgH}_2$  (white) is observed, which is identified by the selected area diffraction patterns given in Figures 9b and 9c, respectively. The  $\text{CeH}_{2.73}$  platelet is of an average width of 15 nm and a planar length of about 100 nm, while the  $\text{MgH}_2$  matrix is nanocrystalline with an average grain size of about 30 nm. It should be pointed out that the  $\text{MgH}_2$  is unstable under ultrahigh vacuum and will decompose into Mg and  $\text{H}_2$  especially when exposes to the electron beam of TEM.

The formation mechanism of the above nanocomposites can be revealed by TEM analysis on the partially hydrogenated  $\text{Mg}_{80}\text{Ce}_{18}\text{Ni}_2$  alloy. Figure 10a is a TEM image of partially

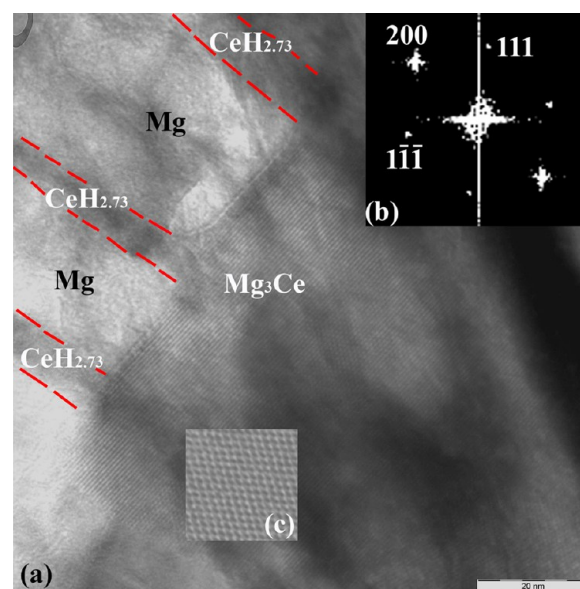


**Figure 10.** TEM images of partially hydrogenated  $\text{Mg}_{80}\text{Ce}_{18}\text{Ni}_2$  alloy. (a) Bright field image, (b) corresponding FFT patterns of  $\text{Mg}_3\text{Ce}$  (zone axis  $[01\bar{1}]$ ), and (c) magnified HRTEM image of  $\text{Mg}_3\text{Ce}$ . When hydrogen reacts with  $\text{Mg}_3\text{Ce}$  particles, the Ce atom first disassociates from  $\text{Mg}_3\text{Ce}$  alloy to combine with the hydrogen and form the platelet  $\text{CeH}_{2.73}$  while Mg atoms rearrange themselves and form metallic Mg.

hydrogenated  $\text{Mg}_{80}\text{Ce}_{18}\text{Ni}_2$  alloy. Figures 10b and 10c are the fast Fourier transform pattern and magnified HRTEM image of



Mg<sub>3</sub>Ce compound, respectively. Figure 10a demonstrates that 5 nm wide CeH<sub>2.73</sub> platelets are embedded in the Mg matrix with a grain size of about 25 nm. According to Figure 10a, the mechanism of the nucleation and growth of the *in situ* formed CeH<sub>2.73</sub>-MgH<sub>2</sub>-Ni composites is somewhat like the pearlite formation in eutectoid steel.<sup>58</sup> When hydrogen reacted with Mg<sub>3</sub>Ce particles, the Ce atoms first disassociate from Mg<sub>3</sub>Ce alloy to combine with the hydrogen and form the platelet CeH<sub>2.73</sub> (see the Supporting Information, Figure S4a). As the CeH<sub>2.73</sub> plate forms, the Mg<sub>3</sub>Ce is depleted of Ce and forms metallic Mg in the area adjacent to the CeH<sub>2.73</sub> plates. The reaction usually takes place initially from the Mg<sub>3</sub>Ce grain boundary and then to the grain center. The growth process of CeH<sub>2.73</sub> and Mg from the Mg<sub>80</sub>Ce<sub>18</sub>Ni<sub>2</sub> leads to the decomposition of the Mg<sub>3</sub>Ce phase and the formation of alternate layers of Mg and CeH<sub>2.73</sub>. This result is different from earlier studies, in which a direct disproportionation to LaH<sub>3</sub> and MgH<sub>2</sub> from both LaMg<sub>12</sub> and La<sub>2</sub>Mg<sub>17</sub> which is suggested on the basis of *in situ* XRD data.<sup>59</sup> This may be due to the sensitivity and time resolution of the conventional XRD not being high enough to identify the medium disproportionation process. The much higher sensitivity and time resolution of the *in situ* synchrotron radiation XRD result reported recently shows that both LaMg<sub>12-x</sub> compound and La<sub>2</sub>Mg<sub>17</sub> react with hydrogen and lead to its disproportionation into LaH<sub>3</sub> hydride and Mg metal.<sup>47,60</sup> This agrees well with the present TEM observations. In addition, the Ni from the decomposition of CeMgNi<sub>4</sub> forms at the boundary between CeH<sub>2.73</sub> and Mg, which is shown in Figure 11. This is the main reason why the grain size of CeH<sub>2.73</sub> and MgH<sub>2</sub> phases is much smaller in the hydrogenated Mg<sub>80</sub>Ce<sub>18</sub>Ni<sub>2</sub> alloy compared to that in the Mg<sub>3</sub>Ce alloy because the very fine CeH<sub>2.73</sub> and Ni phases inhibit the growth of Mg. Consequently, after the Mg<sub>80</sub>Ce<sub>18</sub>Ni<sub>2</sub> alloy has transformed to Mg-CeH<sub>2.73</sub>-Ni, Mg reacts with

hydrogen to form MgH<sub>2</sub> and the *in situ* formed CeH<sub>2.73</sub>-MgH<sub>2</sub>-Ni composites are obtained (see the Supporting Information, Figure S4b).

Based on the above discussion, the great improvement in the hydrogenation kinetics is due to the presence of numerous Ni nanoparticles, high-density interfaces between CeH<sub>2.73</sub> and MgH<sub>2</sub>, and grain boundaries in nanocrystalline MgH<sub>2</sub> in the Mg-CeH<sub>2.73</sub>-Ni composites. These interfaces and boundaries act as H diffusion channels and nucleation sites of hydrides. In addition, the *in situ* formed Ni and CeH<sub>2.73</sub>/CeH<sub>2</sub> phases, with more homogeneity and finer sizes, act as more effective catalysts for the hydriding/dehydriding reaction of Mg and improve more significantly the hydrogenation kinetics in the CeH<sub>2.73</sub>-MgH<sub>2</sub>-Ni composites compared to other catalysts (e.g., FeTi, Mg<sub>2</sub>Ni, LaNi<sub>5</sub>).<sup>17,61–63</sup>

For the dehydrogenation process, the microstructure of the partially dehydrogenated CeH<sub>2.73</sub>-MgH<sub>2</sub>-Ni is also observed by TEM. Figure 11a shows the TEM images of the microstructure. The CeH<sub>2.73</sub>, marked as the white arrow, is embedded in Mg phases (black arrow), while the Ni nanoparticles exist at the boundaries of the CeH<sub>2.73</sub> and MgH<sub>2</sub> phases in the partially dehydrogenated CeH<sub>2.73</sub>-MgH<sub>2</sub>-Ni nanocomposites. The presence of Mg and the remaining MgH<sub>2</sub> is proved by the diffraction patterns of MgH<sub>2</sub> as shown in Figure 11b, and the HRTEM image of Mg can be seen in the inserted picture in Figure 11a. The CeH<sub>2.73</sub> and Ni are identified by EDX using a selective illumination of the respective particles with the focused nano-electron beam of the JEOL-2100 TEM. As shown in Figure 11a, Mg grains, such as those labeled Mg1 and Mg2, can be observed adjacent to the CeH<sub>2.73</sub> and Ni phases, respectively, preferentially nucleates along the interface of CeH<sub>2.73</sub>/CeH<sub>2</sub> and Ni phase in the initial transition stage from MgH<sub>2</sub> to Mg during the dehydrogenation process. This clarifies that the CeH<sub>2.73</sub>/CeH<sub>2</sub> and Ni interfaces act as preferential sites for Mg heterogeneous nucleation from MgH<sub>2</sub> phase. This preferential nucleation confirms that the presence of the *in situ* formed Ni nanoparticles and CeH<sub>2.73</sub> play a catalytic role for improving the dehydrogenation properties.

It should be noted that Ni is observed to exist as pure Ni in the CeH<sub>2.73</sub>-MgH<sub>2</sub>-Ni composites. It is unusual that no Mg<sub>2</sub>Ni formed in such composites and this is totally different from the findings of other Mg-RE-Ni alloys reported by other groups.<sup>64–67</sup> This raises questions why the pure Ni can be formed in the CeH<sub>2.73</sub>-MgH<sub>2</sub>-Ni composites and why Ni can be stable during the hydrogenation/dehydrogenation process. First, Ni is produced from the CeMgNi<sub>4</sub> compound due to the disproportionation reaction. The hydrogenation of CeMgNi<sub>4</sub> leading to the formation of CeH<sub>2.73</sub>, CeH<sub>2.52</sub>, and Ni is also confirmed by other methods such as XRD, neutron diffraction, and *ab initio* calculations using pseudopotential and all-electron DFT methods.<sup>68</sup> Second, an *in situ* XRD study of the hydriding combustion synthesis of Mg<sub>2</sub>NiH<sub>4</sub> has shown that no Mg<sub>2</sub>Ni can be formed below 633 K.<sup>69</sup> In other words, Ni and Mg are stable under hydrogen atmospheric pressure below 633 K. Because all the measurements on CeH<sub>2.73</sub>-MgH<sub>2</sub>-Ni composites have been performed below 590 K in this work, it is reasonable that the pure Ni remains stable.

To further clarify the effect of Ni on microstructure stability and catalysis, the hydrogenated Mg<sub>3</sub>Ce alloy is also characterized using TEM for comparison. Figure 12a is a bright field image of *in situ* formed MgH<sub>2</sub>-CeH<sub>2.73</sub> composites, and Figure 12b is dark field image of CeH<sub>2.73</sub>. Figures 12c and 12d are selected area diffraction patterns of CeH<sub>2.73</sub> (zone axis

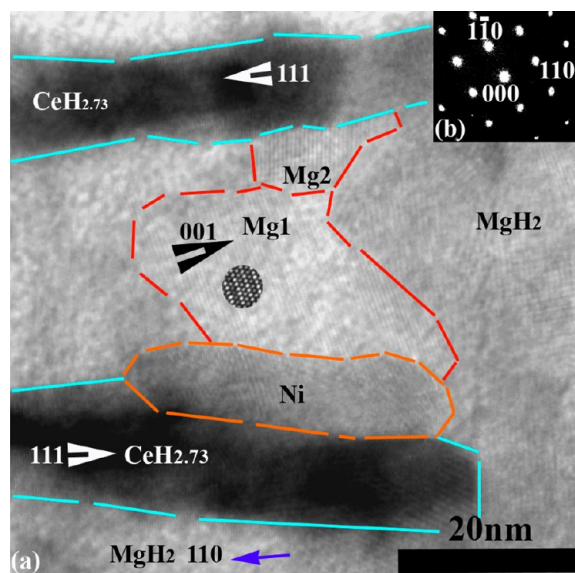


**Figure 11.** TEM images of the microstructure of the partially dehydrogenated CeH<sub>2.73</sub>-MgH<sub>2</sub>-Ni nanocomposites demonstrate the catalyst effect of CeH<sub>2.73</sub> and Ni on MgH<sub>2</sub> dehydrogenation process. (a) Bright field image of the *in situ* formed CeH<sub>2.73</sub>-MgH<sub>2</sub>-Ni composite and (b) selected area diffraction patterns of MgH<sub>2</sub> (zone axis [011]). Mg nuclei preferentially nucleate along the surface of CeH<sub>2.73</sub>/CeH<sub>2</sub> and Ni phase at the starting transition stage of MgH<sub>2</sub> to Mg during the dehydrogenation process.



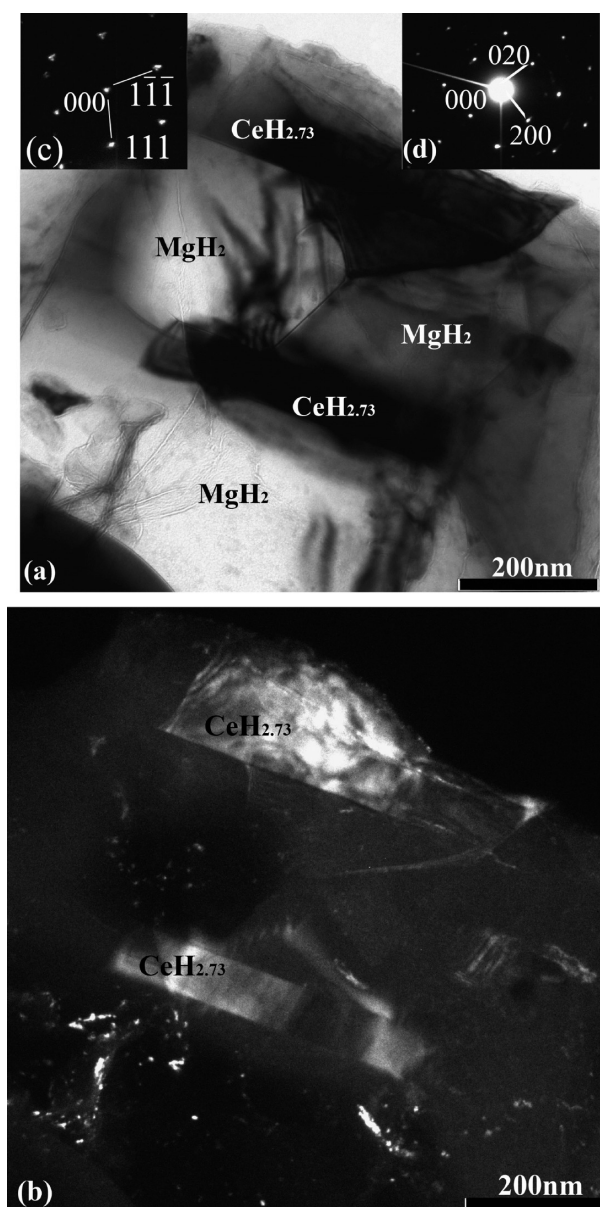


**Figure 12.** TEM images of *in situ* formed  $\text{MgH}_2\text{-CeH}_{2.73}$  composite. (a) Bright field image, (b) dark field image of  $\text{CeH}_{2.73}$ , (c) selected area diffraction patterns of  $\text{CeH}_{2.73}$  (zone axis  $[01\bar{1}]$ ), and (d) tetragonal  $\text{MgH}_2$  (zone axis  $[001]$ ). The  $\text{Mg}_3\text{Ce}$  alloy reacts with hydrogen at 298 K and forms  $\text{MgH}_2\text{-CeH}_{2.73}$  composites with a unique microstructure of the  $\text{MgH}_2$  and  $\text{CeH}_{2.73}$  alternative distribution.

$[01\bar{1}]$ ) and (d) tetragonal  $\text{MgH}_2$  (zone axis  $[001]$ ), respectively. The dark field image is obtained by selecting the diffraction spots of  $\text{CeH}_{2.73}$  (Figure 12c). The  $\text{CeH}_{2.73}$  platelets roughly had a width of about 80 nm and a length of about 400 nm and embedded in the  $\text{MgH}_2$  matrix of a grain size of about 200 nm. Although the  $\text{CeH}_{2.73}\text{-MgH}_2$  composites have a lamellar structure similar to  $\text{CeH}_{2.73}\text{-MgH}_2\text{-Ni}$  composites, the size of both  $\text{MgH}_2$  and  $\text{CeH}_{2.73}$  phases in  $\text{CeH}_{2.73}\text{-MgH}_2$  composites is much bigger than that of the  $\text{CeH}_{2.73}\text{-MgH}_2\text{-Ni}$  composites. This result shows that Ni introduced is a key role for refining the microstructure of  $\text{CeH}_{2.73}\text{-MgH}_2$  composites, which is beneficial for the kinetic improvement. Previous studies have shown that a reduction in particle size is favorable for hydrogen absorption of Mg.<sup>71,72</sup> Furthermore, the *in situ* formed hydrides are isolated from oxygen and other possible

hazardous gases, thus preventing the Mg particle surfaces from oxidizing. The homogeneous distribution of the rare-earth hydrides could also increase the interface density, which significantly increases the number of hydrogen diffusion channels and favors the hydrogen absorption/desorption kinetics. Furthermore, Ni not only demonstrates good catalytic effects on the hydrogen desorption of  $\text{MgH}_2$  but also enables the transformation of  $\text{CeH}_{2.73}$  to  $\text{CeH}_2$  as revealed by the XRD in Figure 1d. This transformation contributes to the increase of hydrogen desorption capacity.

#### 4. CONCLUSIONS

This work tries to combine the catalytic effect of *in situ* formed Ni nanoparticles and “hydrogen pump” effect of  $\text{CeH}_{2.73}$  on an *in situ* formed Mg particles with fine grains. The strategy is through the hydrogenation of  $\text{Mg}_{80}\text{Ce}_{18}\text{Ni}_2$  alloy to form  $\text{CeH}_{2.73}\text{-MgH}_2\text{-Ni}$  composites, in which the *in situ* formed Ni nanoparticles locate on the grain boundaries of  $\text{CeH}_{2.73}/\text{Mg}$  particles. The nanoscale Ni particles then restrict the movement of the grain boundaries, thus limiting the growth of grains. The nanocomposites exhibit excellent hydrogen absorption/desorption performance and cycling stability, which can absorb hydrogen at room temperature and desorb hydrogen at 505 K with a high capacity of  $\sim 4$  wt % and fast kinetics. The apparent activation energy ( $E_a$ ) is only  $63 \pm 3$  kJ/mol  $\text{H}_2$ , which is far below that of milled  $\text{MgH}_2$  ( $\sim 158$  kJ/mol  $\text{H}_2$ ), ascribed to contribution on the fast kinetics. In addition, the existence of *in situ* formed Ni enables the reaction of  $\text{CeH}_{2.73}$  to  $\text{CeH}_2$ , which contributes a higher practical hydrogen capacity. The hydrogen capacity can remain up to 80% after 500 hydrogenation/dehydrogenation cycles, and the main reason for the capacity loss is by the oxidation.

#### ■ ASSOCIATED CONTENT

##### Supporting Information

Figure showing hydrogen thermal desorption traces from  $\text{CeH}_{2.73}$  hydride, XRD patterns of  $\text{CeH}_{2.73}$  hydride, and  $\text{CeH}_2$  hydride dehydrogenated from  $\text{CeH}_{2.73}$  hydride in vacuum at 663 K, the Van't Hoff plots of  $\text{CeH}_{2.73}\text{-MgH}_2\text{-Ni}$  composites measured at different cycles of hydrogenation/dehydrogenation, and schematic representation of the microstructure evolution for the *in situ* formed  $\text{CeH}_{2.73}\text{-MgH}_2\text{-Ni}$  composite. This material is available free of charge via the Internet at <http://pubs.acs.org>.

#### ■ AUTHOR INFORMATION

##### Corresponding Authors

\*E-mail [memzhu@scut.edu.cn](mailto:memzhu@scut.edu.cn) (M.Z.).

\*E-mail [x.yao@griffith.edu.au](mailto:x.yao@griffith.edu.au) (X.D.Y.).

##### Notes

The authors declare no competing financial interest.

#### ■ ACKNOWLEDGMENTS

This work was financially supported by the Ministry of Science and Technology of China (No. 2010CB631302), the National Natural Science Foundation of China (Nos. U1201241, 51271078, and 50925102), and KLGHEI (KLB11003). The financial assistance from Australian Research Council (ARC) is also acknowledged.

## REFERENCES

- (1) Vons, V. A.; Anastasopol, A.; Legerstee, W. J.; Mulder, F. M.; Eijt, S. W. H.; Schmidt-Ott, A. Low-temperature hydrogen desorption and the structural properties of spark discharge generated Mg nanoparticles. *Acta Mater.* **2011**, *59*, 3070–3080.
- (2) Danaie, M.; Tao, S. X.; Kalisvaart, P.; Mitlin, D. Analysis of deformation twins and the partially dehydrogenated microstructure in nanocrystalline magnesium hydride (MgH<sub>2</sub>) powder. *Acta Mater.* **2010**, *58*, 3162–3172.
- (3) Ouyang, L. Z.; Ye, S. Y.; Dong, H. W.; Zhu, M. Effect of interfacial free energy on hydriding reaction of Mg–Ni thin films. *Appl. Phys. Lett.* **2007**, *90*, 021917–021917–3.
- (4) Cuevas, F.; Fernández, J. F.; Ares, J. R.; Leardini, F.; Sánchez, C. Homogeneity range and crystal structure of Ni substituted Mg<sub>6</sub>(Pd, Ni) complex intermetallic compounds. *J. Phys. Chem. Solids* **2010**, *71*, 1259–1263.
- (5) Danaie, M.; Mitlin, D. TEM analysis of the microstructure in TiF<sub>3</sub>-catalyzed and pure MgH<sub>2</sub> during the hydrogen storage cycling. *Acta Mater.* **2012**, *60*, 6441–6456.
- (6) Kalisvaart, W. P.; Kubis, A.; Danaie, M.; Amirkhiz, B. S.; Mitlin, D. Microstructural evolution during hydrogen sorption cycling of Mg–FeTi nanolayered composites. *Acta Mater.* **2011**, *59*, 2083–2095.
- (7) Hu, J. J.; Röhm, E.; Fichtner, M. Feasibility and performance of the mixture of MgH<sub>2</sub> and LiNH<sub>2</sub>(1:1) as a hydrogen-storage material. *Acta Mater.* **2011**, *59*, 5821–5831.
- (8) Zaluski, L.; Zaluska, A.; Tessier, P.; Strom-Olsen, J. O.; Schulz, R. Catalytic effect of Pd on hydrogen absorption in mechanically alloyed Mg<sub>2</sub>Ni, LaNi<sub>5</sub> and FeTi. *J. Alloys Compd.* **1995**, *217*, 295–300.
- (9) Gross, K. J.; Spatz, P.; Züttel, A.; Schlapbach, L. Mechanically milled Mg composites for hydrogen storage the transition to a steady state composition. *J. Alloys Compd.* **1996**, *240*, 206–213.
- (10) Liang, G.; Boily, S.; Huot, J.; Van Neste, A.; Schulz, R. Mechanical alloying and hydrogen absorption properties of the Mg–Ni system. *J. Alloys Compd.* **1998**, *267*, 302–306.
- (11) Li, W. Y.; Li, C. S. Magnesium nanowires: Enhanced kinetics for hydrogen absorption and desorption. *J. Am. Chem. Soc.* **2007**, *129*, 6710–6711.
- (12) Nielsen, T. K.; Manickam, K.; Hirscher, M.; Besenbacher, F.; Jensen, T. R. Confinement of MgH<sub>2</sub> nanoclusters within nanoporous aerogel scaffold materials. *ACS Nano* **2009**, *3*, 3521–3528.
- (13) Zhang, K.; Rossi, C.; Tenaillon, C.; Alphonse, P. Aligned three-dimensional prismlike magnesium nanostructures realized onto silicon substrate. *Appl. Phys. Lett.* **2008**, *92*, 063123.
- (14) De Jongh, P. E.; Wagemans, R. W. P.; Eggenhuisen, T. M.; Dauvillier, B. S.; Radstake, P. B.; Meeldijk, J. D.; Geus, J. W.; De Jong, K. P. The preparation of carbon-supported magnesium nanoparticles using melt infiltration. *Chem. Mater.* **2007**, *19*, 6052–6057.
- (15) Paskevicius, M.; Sheppard, D. A.; Buckley, C. E. Thermodynamic changes in mechanochemically synthesized magnesium hydride nanoparticles. *J. Am. Chem. Soc.* **2010**, *132*, 5077–5083.
- (16) Qu, J.; Sun, B.; Zheng, J.; Yang, R.; Wang, Y.; Li, X. Hydrogen desorption properties of Mg thin films at room temperature. *J. Power Sources* **2010**, *195*, 1190–1194.
- (17) Dornheim, M.; Doppiu, S.; Barkhordarian, G.; Boesenberg, U.; Klassen, T.; Gutfleisch, O.; Bormann, R. Hydrogen storage in magnesium-based hydrides and hydride composites. *Scr. Mater.* **2007**, *56*, 841–846.
- (18) Denys, R. V.; Riabov, A. B.; Maehlen, J. P.; Lototsky, M. V.; Solberg, J. K.; Yartys, V. A. In situ synchrotron X-ray diffraction studies of hydrogen desorption and absorption properties of Mg and Mg–Mn–Ni after reactive ball milling in hydrogen. *Acta Mater.* **2009**, *57*, 3989–4000.
- (19) Oelerich, W.; Klassen, T.; Bormann, R. Metal oxides as catalysts for improved hydrogen sorption in nanocrystalline Mg-based materials. *J. Alloys Compd.* **2001**, *315*, 237–242.
- (20) Reimann, A. L. The clean-up of hydrogen by magnesium. *Philos. Mag.* **1933**, *16*, 673–686.
- (21) Yu, X. B.; Yang, Z. X.; Liu, H. K.; Grant, D. M.; Walker, G. S. The effect of a Ti–V-based BCC alloy as a catalyst on the hydrogen storage properties of MgH<sub>2</sub>. *Int. J. Hydrogen Energy* **2010**, *35*, 6338–6344.
- (22) Guvendiren, M.; Bayboru, E.; Ozturk, T. Effects of additives on mechanical milling and hydrogenation of magnesium powders. *Int. J. Hydrogen Energy* **2004**, *29*, 491–496.
- (23) Jin, S. A.; Shim, J. H.; Ahn, J. P.; Cho, Y. W.; Yi, K. W. Improvement in hydrogen sorption kinetics of MgH<sub>2</sub> with Nb hydride catalyst. *Acta Mater.* **2007**, *55*, 5073–5079.
- (24) Lu, J.; Choi, Y. J.; Fang, Z. Z.; Sohn, H. Y.; Rönnebro, E. Hydrogen storage properties of nanosized MgH<sub>2</sub>–0.1TiH<sub>2</sub> prepared by ultrahigh-energy-high-pressure milling. *J. Am. Chem. Soc.* **2009**, *131*, 15843–15852.
- (25) Cuevas, F.; Korablov, D.; Latroche, M. Synthesis, structural and hydrogenation properties of Mg-rich MgH<sub>2</sub>–TiH<sub>2</sub> nanocomposites prepared by reactive ball milling under hydrogen gas. *Phys. Chem. Chem. Phys.* **2012**, *14*, 1200–1211.
- (26) Bambhaniya, K. G.; Grewal, G. S.; Shrinet, V.; Singh, N. L.; Govindan, T. P. Fast hydriding Mg–Zr–Mn–Ni alloy compositions for high capacity hydrogen storage application. *Int. J. Hydrogen Energy* **2012**, *37*, 3671–3676.
- (27) Mohammad, R. E.; Mahmoud, H. S.; Abdolghayoom, S. Liquid phase surface alloying of AZ91D magnesium alloy with Al and Ni powders. *Appl. Surf. Sci.* **2012**, *258*, S876–S880.
- (28) Wang, P.; Kang, X. D.; Cheng, H. M. Exploration of the nature of active Ti species in metallic Ti-doped NaAlH<sub>4</sub>. *J. Phys. Chem. B* **2005**, *109*, 20131–20136.
- (29) Gennari, F. C.; Fernandez, A. L.; Puszekiel, J. A.; Larochette, P. A. Reversible hydrogen storage from 6LiBH<sub>4</sub>–MCl<sub>3</sub> (M=Ce, Gd) composites by in-situ formation of MH<sub>2</sub>. *Int. J. Hydrogen Energy* **2011**, *36*, 563–570.
- (30) Norskov, J. K.; Hammer, B. Why gold is the noblest of all the metals. *Nature* **1995**, *376*, 238–240.
- (31) Harris, J.; Anderson, S. Dissociation at metal surfaces. *Phys. Rev. Lett.* **1985**, *55*, 1583–1586.
- (32) Chen, M.; Cai, Z. Z.; Yang, X. B.; Zhu, M.; Zhao, Y. J. Theoretical study of hydrogen dissociation and diffusion on Nb and Ni co-doped Mg(0001): A synergistic effect. *Surf. Sci.* **2012**, *606*, L45–L49.
- (33) Poletaev, A. A.; Denys, R. V.; Maehlen, J. P.; Solberg, J. K.; Tarasov, B. P.; Yartys, V. A. Nanostructured rapidly solidified LaMg<sub>11</sub>Ni alloy: Microstructure, crystal structure and hydrogenation properties. *Int. J. Hydrogen Energy* **2012**, *37*, 3548–3557.
- (34) Zhou, Y. F.; Liu, Y. F.; Wu, W.; Zhang, Y.; Gao, M. X.; Pan, H. G. Improved hydrogen storage properties of LiBH<sub>4</sub> destabilized by in situ formation of MgH<sub>2</sub> and LaH<sub>3</sub>. *J. Phys. Chem. C* **2012**, *116*, 1588–1595.
- (35) Lin, H. J.; Ouyang, L. Z.; Wang, H.; Zhao, D. Q.; Wang, W. H.; Sun, D. L.; Zhu, M. Hydrogen storage properties of Mg–Ce–Ni nanocomposite induced from amorphous precursor with the highest Mg content. *Int. J. Hydrogen Energy* **2012**, *37*, 14329–14335.
- (36) Berlouis, L. E. A.; Honnor, P.; Hall, P. J.; Morris, S.; Dodd, S. B. An investigation of the effect of Ti, Pd and Zr on the dehydriding kinetics of MgH<sub>2</sub>. *J. Mater. Sci.* **2006**, *41*, 6403–6408.
- (37) Pezat, M.; Darriet, B.; Hagenmuller, P. A comparative study of magnesium-rich rare-earth-based alloys for hydrogen storage. *J. Less-Common Met.* **1980**, *74*, 427–434.
- (38) Liu, J.; Zhang, X.; Li, Q.; Chou, K. C.; Xu, K. D. Investigation on kinetics mechanism of hydrogen absorption in the La<sub>2</sub>Mg<sub>17</sub>-based composites. *Int. J. Hydrogen Energy* **2009**, *34*, 1951–1957.
- (39) Lu, Z. W.; Wang, G.; Gao, X. P.; Liu, X. J.; Wang, J. Q. Electrochemical performance of Si–CeMg<sub>12</sub> composites as anode materials for Li-ion batteries. *J. Power Sources* **2009**, *189*, 832–836.
- (40) Denys, R. V.; Poletaev, A. A.; Maehlen, J. P.; Solberg, J. K.; Tarasov, B. P.; Yartys, V. A. Nanostructured rapidly solidified LaMg<sub>11</sub>Ni alloy. II. In situ synchrotron X-ray diffraction studies of hydrogen absorption–desorption behaviours. *Int. J. Hydrogen Energy* **2012**, *37*, 5710–5722.
- (41) Denys, R. V.; Poletaev, A. A.; Solberg, J. K.; Tarasov, B. P.; Yartys, V. A. LaMg<sub>11</sub> with a giant unit cell synthesized by hydrogen

- metallurgy: Crystal structure and hydrogenation behavior. *Acta Mater.* **2010**, *58*, 2510–2519.
- (42) Zlotea, C.; Sahlberg, M.; Özbilen, S.; Moretto, P.; Andersson, Y. Hydrogen desorption studies of the Mg<sub>2</sub>Y<sub>5</sub>-H system: Formation of Mg tubes, kinetics and cycling effects. *Acta Mater.* **2008**, *56*, 2421–2428.
- (43) Ouyang, L. Z.; Qin, F. X.; Zhu, M. The hydrogen storage behavior of Mg<sub>3</sub>La and Mg<sub>3</sub>LaNi<sub>0.1</sub>. *Scr. Mater.* **2006**, *55*, 1075–1078.
- (44) Ouyang, L. Z.; Dong, H. W.; Peng, C. H.; Sun, D. L.; Zhu, M. A new type of Mg-based metal hydride with promising hydrogen storage properties. *Int. J. Hydrogen Energy* **2007**, *32*, 3929–3935.
- (45) Sun, T.; Wang, H.; Zhang, Q. A.; Sun, D. L.; Yao, X. D.; Zhu, M. Synergetic effects of hydrogenated Mg<sub>3</sub>La and TiCl<sub>3</sub> on the dehydrogenation of LiBH<sub>4</sub>. *J. Mater. Chem.* **2011**, *21*, 9179–9184.
- (46) Bobet, J. L.; Grigorova, E.; Chevalier, B.; Khrussanova, M.; Peshev, P. Hydrogenation of CeNi: hydride formation, structure and magnetic properties. *Intermetallics* **2006**, *14*, 208–212.
- (47) Denys, R. V.; Poletaev, A. A.; Solberg, J. K.; Tarasov, B. P.; Yartys, V. A. LaMg<sub>11</sub> with a giant unit cell synthesized by hydrogen metallurgy: Crystal structure and hydrogenation behavior. *Acta Mater.* **2010**, *58*, 2510–2519.
- (48) Barkhordarian, G.; Klassen, T.; Bormann, R. Kinetic investigation of the effect of milling time on the hydrogen sorption reaction of magnesium catalyzed with different Nb<sub>2</sub>O<sub>5</sub> contents. *J. Alloys Compd.* **2006**, *407*, 249–255.
- (49) Zhu, M.; Gao, Y.; Che, X. Z.; Yang, Y. Q.; Chung, C. Y. Hydriding kinetics of nano-phase composite hydrogen storage alloys prepared by mechanical alloying of Mg and MmNi<sub>5-x</sub>(CoAlMn)<sub>x</sub>. *J. Alloys Compd.* **2002**, *330*, 708–713.
- (50) Liu, Y. F.; Zhong, K.; Luo, K.; Gao, M. X.; Pan, H. G.; Wang, Q. D. Size-Dependent Kinetic Enhancement in Hydrogen Absorption and Desorption of the Li-Mg-N-H System. *J. Am. Chem. Soc.* **2009**, *131*, 1862–1870.
- (51) Li, Y.; Zhou, G.; Fang, F.; Yu, X. B.; Zhang, Q. A.; Ouyang, L. Z.; Zhu, M.; Sun, D. L. De-/re-hydrogenation features of NaAlH<sub>4</sub> confined exclusively in nanopores. *Acta Mater.* **2011**, *59*, 1829–1838.
- (52) Huot, J.; Liang, G.; Boily, S.; Van Neste, A.; Schulz, R. Structural study and hydrogen sorption kinetics of ball-milled magnesium hydride. *J. Alloys Compd.* **1999**, *293*, 495–500.
- (53) Fernandez, J. F.; Sanchez, C. R. Rate determining step in the absorption and desorption of hydrogen by magnesium. *J. Alloys Compd.* **2002**, *340*, 189–198.
- (54) Mao, J.; Guo, Z.; Yu, X.; Liu, H.; Wu, Z.; Ni, J. Enhanced hydrogen sorption properties of Ni and Co-catalyzed MgH<sub>2</sub>. *Int. J. Hydrogen Energy* **2010**, *35*, 4569–4575.
- (55) Huot, J.; Pelletier, J. F.; Lurio, L. B.; Sutton, M.; Schulz, R. Investigation of dehydrogenation mechanism of MgH<sub>2</sub>-Nb nanocomposites. *J. Alloys Compd.* **2003**, *348*, 319–324.
- (56) Liang, G.; Huot, J.; Boily, S.; Schulz, R. Hydrogen desorption kinetics of a mechanically milled MgH<sub>2</sub> + 5 atom % V nanocomposite. *J. Alloys Compd.* **2000**, *305*, 239–245.
- (57) Bobet, J. L.; Grigorova, E.; Chevalier, B.; Khrussanova, M.; Peshev, P. Hydrogenation of CeNi: hydride formation, structure and magnetic properties. *Intermetallics* **2006**, *14*, 208–212.
- (58) Ande, C. K.; Sluiter, M. H. F. First-principles prediction of partitioning of alloying elements between cementite and ferrite. *Acta Mater.* **2010**, *58*, 6276–6281.
- (59) Sun, D. L.; Ging, F.; Nakamura, Y.; Enoki, H.; Bououdina, M.; Akiba, E. In situ X-ray diffraction study of hydrogen-induced phase decomposition in LaMg<sub>12</sub> and La<sub>2</sub>Mg<sub>17</sub>. *J. Alloys Compd.* **2002**, *333*, 103–108.
- (60) Poletaev, A. A.; Denys, R. V.; Solberg, J. K.; Tarasov, B. P.; Yartys, V. A. Microstructural optimization of LaMg<sub>12</sub> alloy for hydrogen storage. *J. Alloys Compd.* **2011**, *509*, S633–S639.
- (61) Reguera, E. Materials for hydrogen storage in nanocavities: design criteria. *Int. J. Hydrogen Energy* **2009**, *34*, 9163–9167.
- (62) Schlapbach, L.; Züttel, A. Hydrogen-storage materials for mobile applications. *Nature* **2001**, *414*, 353–358.
- (63) Jurczyk, M.; Nowak, M.; Szajek, A.; Jezierski, A. Hydrogen storage by Mg-based nanocomposites. *Int. J. Hydrogen Energy* **2012**, *37*, 3652–3658.
- (64) Denys, R. V.; Riabov, A. B.; Maehlen, J. P.; Lototsky, M. V.; Solberg, J. K.; Yartys, V. A. In situ synchrotron X-ray diffraction studies of hydrogen desorption and absorption properties of Mg and Mg-Mm-Ni after reactive ball milling in hydrogen. *Acta Mater.* **2009**, *57*, 3989–4000.
- (65) Poletaev, A. A.; Denys, R. V.; Maehlen, J. P.; Solberg, J. K.; Tarasov, B. P.; Yartys, V. A. Nanostructured rapidly solidified LaMg<sub>11</sub>Ni alloy: Microstructure, crystal structure and hydrogenation properties. *Int. J. Hydrogen Energy* **2012**, *37*, 3548–3557.
- (66) Denys, R. V.; Poletaev, A. A.; Maehlen, J. P.; Solberg, J. K.; Tarasov, B. P.; Yartys, V. A. Nanostructured rapidly solidified LaMg<sub>11</sub>Ni alloy. II. In situ synchrotron X-ray diffraction studies of hydrogen absorption-desorption behaviours. *Int. J. Hydrogen Energy* **2012**, *37*, 5710–5722.
- (67) Wu, Y.; Lototsky, M. V.; Solberg, J. K.; Yartys, V. A. Effect of microstructure on the phase composition and hydrogen absorption-desorption behaviour of melt-spun Mg-20Ni-8Mm alloys. *Int. J. Hydrogen Energy* **2012**, *37*, 1495–1508.
- (68) Roquefere, J. G.; Matar, S. F.; Huot, J.; Bobet, J. L. X-ray/neutron diffraction studies and ab initio electronic structure of CeMgNi<sub>4</sub> and its hydride. *Solid State Sci.* **2009**, *11*, 1971–1978.
- (69) Li, L. Q.; Akiyama, T.; Kabutomori, T.; Terao, K.; Yagi, J. In situ X-ray diffraction study of the hydriding combustion synthesis of Mg<sub>2</sub>NiH<sub>4</sub>. *J. Alloys Compd.* **1998**, *281*, 175–180.
- (70) Kamegawa, A.; Goto, Y.; Kakuta, H.; Takamura, H.; Okada, M. High-pressure synthesis of novel hydrides in Mg-RE-H systems (RE = Y, La, Ce, Pr, Sm, Gd, Tb, Dy). *J. Alloys Compd.* **2006**, *408*, 284–287.
- (71) Huang, Z. G.; Guo, Z. P.; Calka, A.; Wexler, D.; Liu, H. K. Effects of iron oxide (Fe<sub>2</sub>O<sub>3</sub>, Fe<sub>3</sub>O<sub>4</sub>) on hydrogen storage properties of Mg-based composites. *J. Alloys Compd.* **2006**, *422*, 299–304.
- (72) Jensen, T.; Andreasen, A.; Vegge, T.; Andreasen, J. W.; Stahl, K.; Pedersen, A. Dehydrogenation kinetics of pure and nickel-doped magnesium hydride investigated by in situ time-resolved powder X-ray diffraction. *Int. J. Hydrogen Energy* **2006**, *31*, 2052–2062.